Synaptic Microchannels

Using nonlinear transport in microfluidics and surface chemistry to design fully iontronic memristors with short-term, long-term, frequency-dependent and Hebbian plasticity

Martijn Klop

Master's Thesis Theoretical Physics and Neuroscience and Cognition

Institute for Theoretical Physics
Utrecht University
The Netherlands
July 7th, 2023

Abstract

Charged micro-scale fluid channels display intriguing and non-linear transport phenomena. When forced or integrated in an electric circuit, they display spiking and learning behaviour similar to our neurons and synapses. By adding specific surface chemistry to the walls of these channels, a coupling between charge accumulation, surface charge and conductivity opens up a new spectrum of possibilities for neuromorphic engineering. Specifically, intrinsically non-linear charging dynamics of surface reactions with charged reactants are amplified by the current rectifying behaviour of inhomogeneous channel types, such as cones, creating a semi-independent internal state parameter that changes the conductivity. Among other things, these systems can display near non-volatile memristive properties, frequency dependent plasticity and chemically induced Hebbian learning. Because of their high-level resemblance with the underlying physics and chemistry of synaptic transmission, these systems are promising for use in neuromorphic computing, neural implants and brain-computer interfaces.

Acknowledgements

I want to express my gratitude towards prof. dr. René van Roij and dr. Bodo Rückauer for supervising this project, suggesting improvements and helping me find new ways of moving the project forward and tying it to existing literature. It was exciting to work together with Tim Kamsma, who brought in many new ideas and is on his way to become a very professional, remarkably productive researcher. Lastly, I want to thank Dr. Willem Boon, who's work I built on and who has great patience and clarity when explaining technical topics.

Contents

1 Introduction

Microfluidics is a branch of physics that deals with the behavior of fluids at the microscopic scale, such as fluid channels in the order of micrometers. These systems are useful for a variety of applications, such as biological analysis, sensing [1], drug discovery [2], and environmental monitoring[3]. Due to the small size of the channels or chambers, the fluids in microfluidic systems exhibit different behavior than they would at larger scales. This is due to the fact that in the force balance describing the motion of fluids, the inertia-terms vanish relatively to the other terms, captured in the low Reynolds number of such systems. As a result, surface tension and viscous forces become more significant, and laminar flow is more common [4]

The behavior of objects and fluids in microfluidic systems is often influenced by electric double layers and surface chemistry. The electric double layer is a diffuse layer of positive or negative ionic charges that screen the surface charge from a bulk electrolyte [5]. This layer can affect the way that the liquid flows in response to external forcing and interacts with other substances in the system through electrostatic interactions. Surface chemistry refers to the chemical reactions and interactions that take place at the surface of a solid. This can also influence the behavior of fluids in a microfluidic system, as the surface chemistry of the channels and chambers can affect the surface charge and the interactions between the fluids and the solid surfaces. Understanding and controlling these factors is crucial for successful design and the full exploitation of microfluidic systems.

Microfluidics can be used in the field of iontronics, which is the study and application of electronic devices that use ions rather than electrons for charge transport. In microfluidic iontronic devices, tiny channels and chambers are used to manipulate charged fluids, such as electrolytes or ionic liquids. These fluids can be used as conductive media, allowing for the creation of compact, high-performance iontronic devices [6]. For example, microfluidic iontronic devices have been used to create sensors, actuators, and energy-storage devices, and proposed to be the building blocks for neuromorphic devices. The ability to precisely control and manipulate electrolytes at the microscale allows for the creation of novel iontronic devices with improved performance and functionality [7].

In this thesis, we investigate the application of microfluidic iontronic circuits and components for neuromorphic engineering or computing. Neuromorphic computing is a type of computing that is inspired by the structure and function of the human brain. It involves the use of novel computing architectures and algorithms that are designed to mimic the way that neurons and synapses in the brain process and transmit information. One way that microfluidics can be used in neuromorphic computing is through the use of conical microchannels, which serve as iontronic memristors. Memristors are a type of passive circuit element that can remember the amount of electric charge that has flown through it. In microfluidic iontronic devices, conical microchannels can be used as memristors by controlling the flow of electrolytes through the channels. This allows for the creation of compact, tunable and high-performance memristors that can be used in neuromorphic computing systems.

One area where iontronic systems may be particularly relevant is in the development of brain-computer interfaces (BCIs). BCIs are devices that allow the brain to directly control external devices, such as computers or prosthetic limbs. Iontronic systems may be well-suited for this application, as they can be integrated with biological tissues more easily than electronic systems and can provide the high-resolution and adaptability that is necessary for effective BCIs [8]. Additionally, iontronic systems can be less invasive and have fewer negative side effects than electronic systems, which is important for applications that involve direct interaction with the brain. Another area where iontronics can stand out is in sensing, where the signals going through an electric microchannel carry information on concentrations, concentration gradients and chemical activity. Hence, even though the development of electronic components is extremely advanced, iontronics has very interesting properties and features to add, and might even help us better understand the workings of our brain.

2 Scope and Relevance

In this thesis, we will investigate a broad range of possible applications of conical micro-pores to neuromorphic engineering. In particular, we focus on the ways to use these microchannels to emulate aspects of learning, plasticity and computation as they occur in the brain.

This research is conducted in collaboration with the Soft Matter group in the Institute for Theoretical Physics in Utrecht, under supervision of prof. dr. R. Van Roij. Earlier work from this group has focused on non-linear transport phenomena in charged conical channels or in inhomogeneously charged channels, and showed how spiking neuron models can be devised out of these iontronic memristors. In this research, we will focus mainly on an extention of this research by adding active surface chemistry to these channels (rather than assuming a fixed, homogenous surface charge). We will see that this extension paves the way for many new applications and opportunities to model and mimic biological components, such as a display of Frequency Dependent Plasticity, Chemically Induced Hebbian Learning, Long Term Potentiation and more.

3 A Short Review of Neuromorphics and Synaptic Plasticity

The most well-known and widely-used example of neuromorphic computational methods is the Artificial Neural Network (ANN). ANNs take inspiration from the brain by mimicking its massively parallel and convoluted method of computing. Many versions of ANNs have been used to learn to classify images [9], transcribe speech [10], generate text to solve challenging tasks [11] and drive cars [12]. These ANNs and the learning methods developed to train them, such as Reinforcement Learning, have mainly taken inspiration from the brain in terms of the software they consist of. Not much has changed in terms of the architecture of the machines they were implemented on, except for specialization of components, such as graphical processing units [13]. The latter were used to optimise the massively parallel operation of neural networks, where large, complex tasks are subdivided in small, elementary floating point operations.

The modern field of Neuromorphic Computing aims to take inspiration from the brain on a hardware level by building computer architecture and components that resemble the workings of the brain. A relatively novel class of devices, *Memristors*, have been used for this purpose. Memristors have the interesting property that their conductance changes as a result of the previous signals that ran through them[14]. This is in contrast with the transistor, which needs a separate external signal (a third terminal called the 'gate') to modify its conductance state. Currently, the most common methods of training ANNs or similar software all depend on calculating the optimal update to the systems parameters required to improve performance, and then sending that signal to a device to update it for later use (most notably using 'backpropagation')[15]. The use of memristors can lead to more integration, where processing a signal automatically leads to a type of learning and remembering, as the signal travelling through the memristive devices will leave a change in its weights. This is often called *on-chip* or *online* learning, which is relevant in situations where your systems need to quickly respond and adapt to their environment without access to massive compute or rich data [16]

In this regard, functional memristors resemble two parts that play an essential role in information processing and propagation in the brain: (i) voltage gated ion channels and (ii) chemical synapses. The former will play a central role in the next chapter, but this chapter will briefly discuss the latter.

Chemical synapses form the parts of a neuron where long-range signals are transmitted to and received from other neurons. Generally, in the central nervous system, neurons receive signals at the branches (dendrites) connected to its body (soma), and transmit signals through their axon towards the chemical synapses at the end. Though many type of neural architectures and connections exist, the chemical synapses are generally believed to be one of the most important components for neural transmission, computation and learning[17]. Synapses are remarkably complex, housing over a thousand different functional proteins with intricate signalling pathways. Much of their high-level functioning is related to one of their most important tasks: to adapt and learn[18].

The field of synaptic plasticity studies how the synapses connecting our neurons change their properties over time. Most notably, this field is concerned with the change of *strength* of synapses changes as a result of their electro-chemical activity, although other types of plasticity exist. The *strength* of a synapse refers to how effective one neuron is at stimulating another through that synapse. This feature of synapses is widely believed to be essential for facilitating memory, learning and many other homeostatic and adaptive features of our brains. [19]. Biological neural networks are parallel and interconnected (illustrated in Figure 1bb), some neurons being connected to up to tens of thousands of other ones [20]. It is the associativity and specificity of these connections that determines how these neural networks perform our cognitive tasks.

There seems to be a connection between the associativity of our memory and learning on the one hand and the associativity of learning rules such as spike-time-dependent plasticity (STDP) or

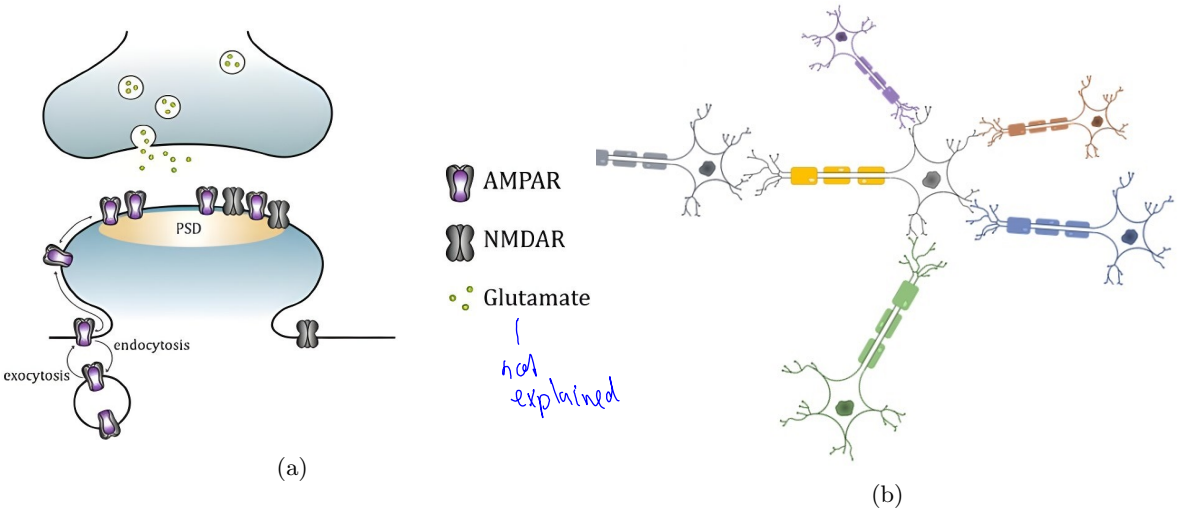

(a) (b)

Figure 1: The roughly 80 billion neurons in the brain are connected to each other by trillions of chemical synapses. (a) At these chemically active clefts between the axon of one neuron and the dendrite of another, neurotransmitters transmit a signal after being released as of a result of an incoming action potential. At the postsynaptic density (PSD), receptors bind these neurotransmitters and become more permeable to sodium (AMPA) or sodium and calcium (NMDA) ions. These receptors are constantly supplied to and taken out of the synapse by exocytosis/endocytosis respectively. (b) Biological neural networks are very interconnected, with many connected neurons contributing to or inhibiting the firing of a single neurons, mainly through chemical axonal-dendritic synapses, although variations exist. [23].

Hebb's rule on the other. This type of plasticity rule governs how the strength of the synapse changes depending on whether the presynaptic neuron contributed to the depolarization of the postsynaptic neuron. The central thesis of STDP is that if a presynaptic neuron fires just before the postsynaptic does, it has likely contributed to its firing, and should do so in the future. If, on the other hand, the presynaptic neuron fires just after the postsynaptic neuron, its signal was either unrelated, or other neurons were better at sending the same signal. In the former case, the synapse will strengthen, and in the latter case, it will weaken [21]. Hebbian plasticity is a more observational rule referring to why and when synapses strengthen and is formulated famously in *Hebb's Rule*: neurons that fire together, wire together.

Biologically, STDP and Hebbian Plasticity in general, are believed to depend on the so-called NMDA receptor's coincidence detection [22] in the common glutametergic synapse. These proteins are ionotropic glutamate receptors (iGluR) found on the postsynaptic membrane and mainly the postsynaptic density (PSD), see Figure 1ba. Upon detection of glutamate and a depolarization of the postsynaptic neuron, they open and permit sodium and calcium to flow into the postsynaptic neuron. Other iGluR's, such as AMPA, open any time whenever glutamate is present in the synaptic cleft, and permit only a sodium influx to cause a depolarization of the postsynaptic neuron, the so-called excitatory postsynaptic potential (EPSP)[17].

Although there are many ways for synapses to restructure or change strength, two commonly studied processes are Long Term Potentiation (LTP) and Long Term Depression (LTD). These processes govern the strength of synapses on the intermediate to long term, by changing the amount and distribution of receptors on the PSD (see Figure 1ba). The receptors on the PSD are continuously supplied by exocytosis and taken away by endocytosis, and their diffusion and distribution across the membrane is also believed to be influenced by internal processes[24]. By changing the balance of

supply and removal, the postsynaptic neuron can change the strength of a synapse [25]. This process is intricate and governed by a host of biological pathways. Notably, intracellular calcium concentrations, governed by the opening and closing of NMDA receptors, are believed to be the main driver of LTP and LTD [26]. Spike timing, co-occurring pre- and postsynaptic activity and pulse-train frequency can all have effects on the transient intracellular calcium concentration. These will be some of the most important factors and learning rules that we will try to model in subsequent sections (see Section 6).

no chapters...

4 The Physics and Memristive Properties of a Conical microchannel

Charged, conical microchannels display filled with an electrolyte (Figure 2) display intruiging transport phenomena, such as current rectification or pressure-sensitive conductance [27]. They are not perfect iontronic diodes, but can display a significant change in conductance dependent on the sign and magnitude of the voltage. The physics of the flow and ionic fluxes inside these devices is described by the Poisson-Nernst-Planck-Stokes (PNPS) system of equations 4.1-4.5.

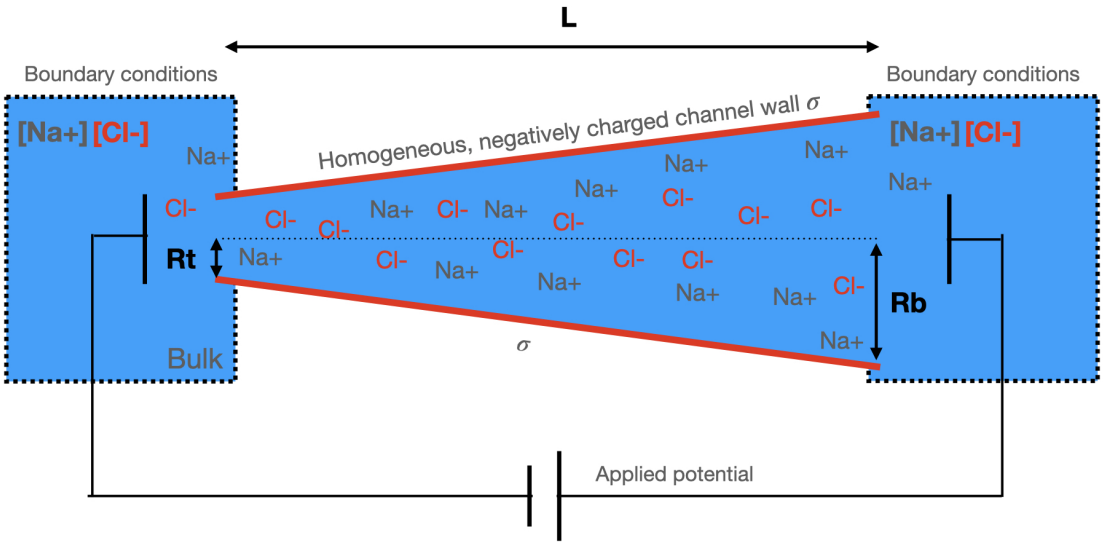

Figure 2: A charged, conical microchannel filled with a 1:1 electrolyte (Na^+:Cl^-). The base and tip radius are on the order of tens to hundred nanometers, and the length in the order if micrometers. Typically, the base and tip radius R_b and R_t have a 4:1 ratio.

Firstly, since we deal with water, an incompressible medium, we demand the velocity field to be divergence free, obeying

$$\nabla \cdot \mathbf{u} = 0. \tag{4.1}$$

Secondly, we expect the velocity field to obey the Stokes equation, which describes the change in momenta as a consequence of viscous forces, pressure gradients and electrical field gradients as

$$\rho_{\mathrm{m}} \frac{\partial \mathbf{u}}{\partial t} = \eta \nabla^2 \mathbf{u} - \nabla P - e\rho_{\mathrm{e}} \nabla \Psi. \tag{4.2}$$

Thirdly, we describe the fluxes of the charge carriers (Na^+ and Cl^-) making up our electrolyte with the continuity relation between density and flux,

$$\frac{\partial \rho_{\pm}}{\partial t} + \nabla \cdot \mathbf{j}_{\pm} = 0, \tag{4.3}$$

and the Nernst-Planck flux balance equation given by

$$\mathbf{j}_{\pm} = -D_{\pm} \left(\nabla \rho_{\pm} \pm \rho_{\pm} \frac{e \nabla \Psi}{k_{\mathrm{B}} T} \right) + \mathbf{u} \rho_{\pm}. \tag{4.4}$$

This last equation describes how ionic fluxes are driven by concentration gradients, electric potential gradients and advection respectively. Lastly, the Poisson equation,

$$\nabla^2 \Psi = -\frac{e}{\epsilon}\rho_e, \tag{4.5}$$

describes the relation between the charge density $\rho_e = \rho_+ - \rho_-$ and the electric field.

Applied to the geometry of a conical channel, where $R(x) = R_b - (R_b - R_t)/L$, and given suitable boundary conditions for the salt concentration ($\rho_i(0) = \rho_i(L) = \rho_{b,i}$), this system of equations is analytically solvable for $\rho_i(x)$ as a function of the external applied potential. Boon et al. (2022) provide a derivation of the solution. In figure 3, we compare these results (AA) to numerical simulations in *Comsol Multiphysics*, a finite element (FE) physics modelling environment.

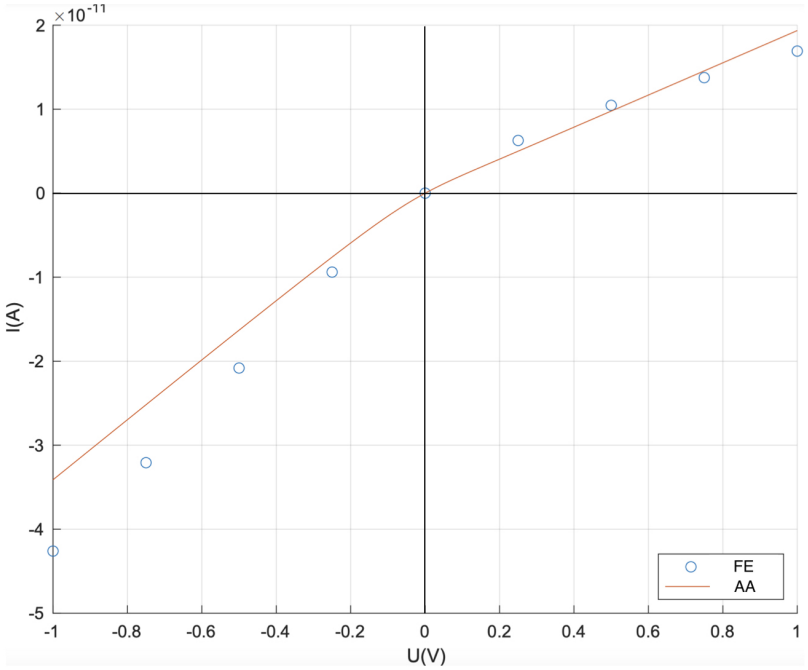

Figure 3: Ionic current rectification in a conical microchannel with dimensions L = 10 μm, Rb = 200 nm, Rt = 50 nm, filled with a monovalent 1:1-electrolyte with ρ_b = 0.5mM. The surface charge is -1e17e/m^2

The current rectification occurs due to the depletion and accumulation of ions in the microchannel and is facilitated by the existence of the electric double layer. This effect can be analytically described by solving the Poisson-Nernst-Planck-Stokes equation [28][29]. We take a cone with a lateral radial profile $R(x) = R_b - (R_b - R_t)/L$, R_b/R_t being the ratio between base and tip radii, and L the length along the longitudinal axis. In it, we describe the ion concentration of a 1:1 electrolyte as $\rho_e(x)$, with boundary conditions $\rho_e(0) = \rho_e(L) = \rho_b$ and define the salt concentration as $\rho_s(x) = \rho_+(x) + \rho_-(x)$. The stationary solution of the laterally averaged salt concentration, with no lateral variation in flow, taken with above boundary conditions, is given by

$$\rho_s(x, V) - 2\rho_b = \frac{\Delta\rho}{\mathrm{Pe}}\left[\frac{x}{L}\frac{R_\mathrm{t}}{R(x)} - \frac{e^{\mathrm{Pe(V)}\frac{x}{L}\frac{R_\mathrm{t}^2}{R_\mathrm{b}R(x)}} - 1}{e^{\mathrm{Pe(V)}\frac{R_\mathrm{t}}{R_\mathrm{b}}} - 1}\right] \mathrm{d}x/L, \tag{4.6}$$

with $\Delta\rho \equiv 2(\Delta R\sigma_0)(e\Delta U_s/k_bTR_t^2)$, Pe the tip Péclet number $\mathrm{Pe} = -(eV/k_\mathrm{B}T)(R_\mathrm{b}/R_\mathrm{t})w^{-1}$ and w a constant $w = eD\eta/(k_\mathrm{B}T\epsilon\psi_0)$. As we know the conductance of our channel to scale roughly linearly with the total average salt concentration in the long-channel and lubrication limit, and taking into account the expression for the equilibrium Ohmic conductance of a conical microchannel $g_0 = (\pi R_\mathrm{t}R_\mathrm{b}/L)(2\rho_\mathrm{b}e^2D/k_\mathrm{B}T)$ we can find the expression for the voltage-dependent conductance to be

$$\frac{g_\infty(V)}{g_0} = 1 + \Delta g \int_0^L \left[\frac{x}{L}\frac{R_\mathrm{t}}{R(x)} - \frac{e^{\mathrm{Pe(V)}\frac{x}{L}\frac{R_\mathrm{t}^2}{R_\mathrm{b}R(x)}} - 1}{e^{\mathrm{Pe(V)}\frac{R_\mathrm{t}}{R_\mathrm{b}}} - 1} \right] \mathrm{d}x/L. \tag{4.7}$$

Here, the Δg is conductance change parameter $\Delta g \equiv -2w(\Delta R/R_b)(\sigma/2\rho_bRt)$. The change in conductance which follows from this accumulation and depletion is not instantaneous with the voltage change, however. It occurs on a timescale $\tau = \frac{L^2}{12D}$, with D the diffusion coefficient of the electrolyte. This can be modelled numerically by letting the conductance evolve according to mono-exponential equilibration as described by

$$\tau\frac{\mathrm{d}g(t)}{\mathrm{d}t} = g_\infty(V(t)) - g(t), \tag{4.8}$$

This then gives rise to the characteristic dynamical behaviour of a conical microchannel filled with an electrolyte: it behaves like a *memristor*. The conductance of the pore now depends on its past voltage trace, as displayed in Figure 4.

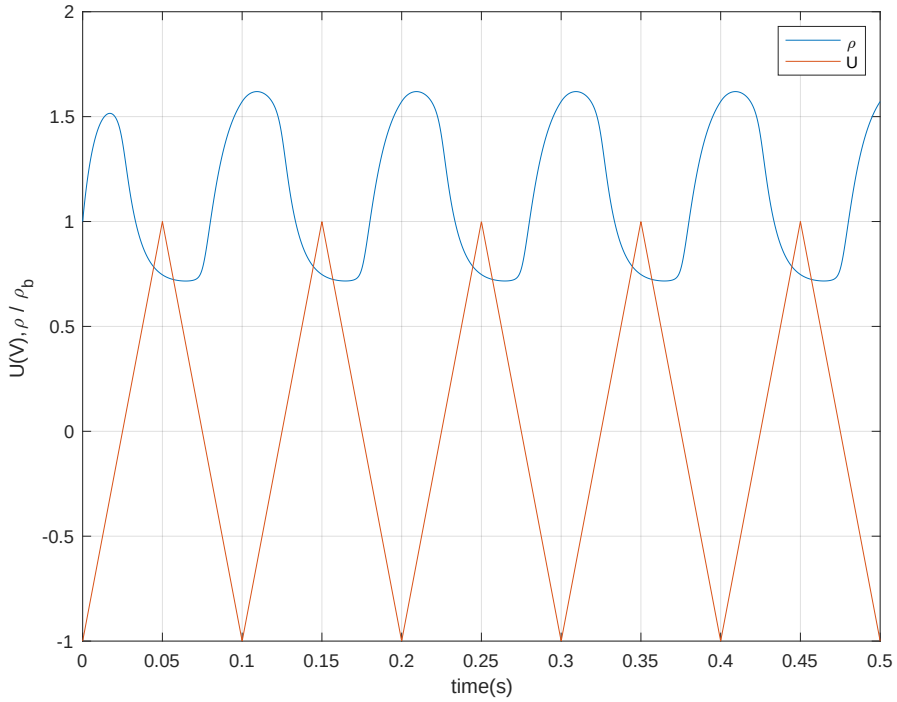

Figure 4: The dynamics of the spatially averaged salt concentration as a proxy for the conductance of the conical microchannel. This figure displays how the salt concentration responds to a sawtooth, alternating potential.

Together, the ionic current rectification and the hysteresis effect gives rise to the pinched hysteresis loop in the voltage-current plane, as displayed in Figure 5. This is a common way to display and analyse memristive behaviour. Figure 5 is the dynamic version of the static current rectification graph

of Figure 3. The enclosed area is what makes memristors different from normal ohmic elements such as passive resistors or diodes. For later application, we again verify the finite-element analysis performed in Comsol Multiphysics with the analytical approximation 4.7 and 4.8.

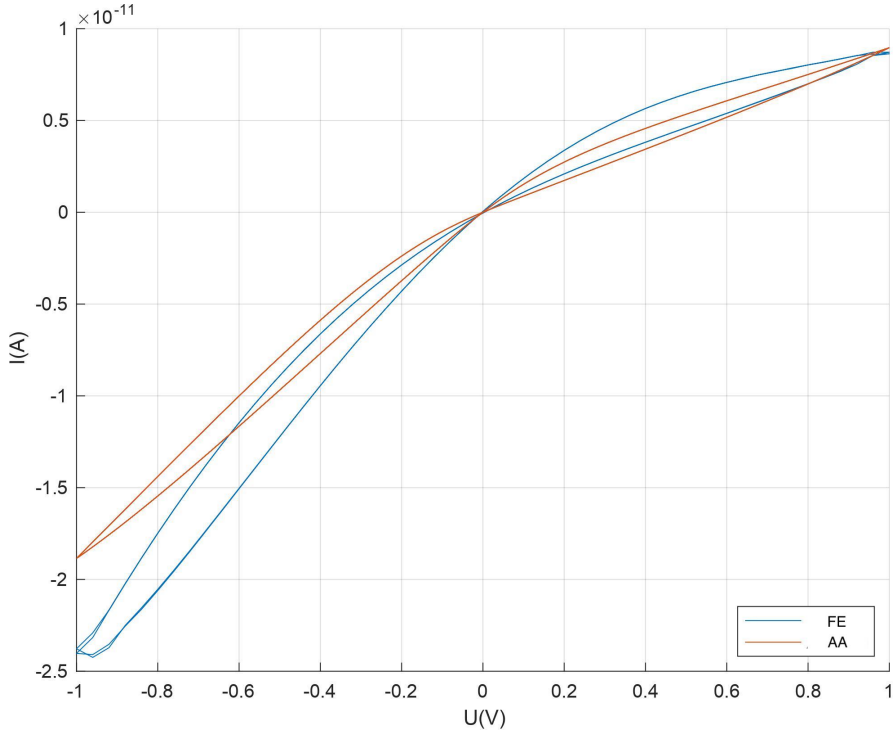

Figure 5: Pinched hysteresis loop in a conical microchannel with dimensions L = 10 μm, Rb = 200 nm, Rt = 50 nm, filled with a monovalent electrolyte with $\rho_b = 0.5$mM under an applied triangle wave potential. Comparison of Finite Element simulations (FE) and Analytical Approximation methods (AA)

5 Neuron models

Neurons are electrically excitable cells that are the building blocks of the nervous system. They are capable of receiving, transmitting, and processing electrical signals, which allows them to perform a wide range of functions, such as sensing the environment, controlling movement, and storing and retrieving information[17]. Neurons can be thought of as dynamical systems, which means that they exhibit complex, nonlinear behavior that is determined by the interactions between their internal states and external forcing[30]. In the case of neurons, this behavior is influenced by a wide range of factors, such as the flow of ions across the cell membrane, the release of neurotransmitters, and the activity of other neurons that the cell is connected to. By understanding the dynamics of neurons, we can gain insight into how the nervous system works and how it is able to perform such a wide range of functions.

The Hodgkin-Huxley circuit is a mathematical model that was developed in the 1950s to describe the electric activity of neurons. The model is a set of equations that describe the flow of ions across the cell membrane of a neuron, and how this flow is influenced by various factors, such as the membrane potential and the concentration of ions inside and outside the cell. The model has been extensively studied and has been found to accurately describe the behavior of neurons in a wide range of situations. It is widely used as a basis for understanding the electric activity of the nervous system.

Although the Hodgkin-Huxley circuit is biologically plausible relative to other mathematical neuron models, its analysis is cumbersome as it consists of four complicated coupled differential equations. This is why many alternative neuron models have been developed since then, that capture some of the excitable properties of a neuron in a simpler system of equations or rules. However, using conical microchannels, it is possible to construct a relatively simple circuit inspired by the Hodgkin-Huxley circuit. This circuit is displayed in Figure 6. It consists of three microchannels with conductivity g_+, g_{slw} and g_- , three respective batteries E_+, E_{slw} and E_-, an applied external current source and a capacitor. Most importantly, the electric potential over the capacitor represents the membrane potential of a biological cell, the element that displays spiking behaviour during an action potential. The labels of the microchannels describe their orientation, plus and minus, and the diffusive timescales relevant for their dynamics. In this case, microchannels '$\pm$' have a length of 2.5 μm and the 'slow' microchannel has a length of 10 μm. As a consequence, the reactive time of the longer channel is 16 times longer than the shorter channels, as

$$\tau \approx \frac{L^2}{12D}, \tag{5.1}$$

is the equation for τ as used in 4.8.

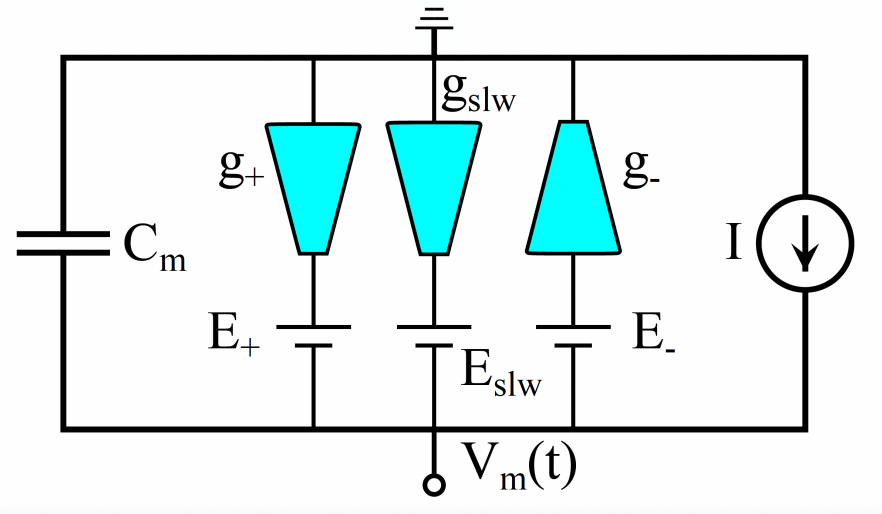

Figure 6: A Hodgkin-Huxley type circuit made of conical microchannels filled with electrolyte.

When we simulate the behaviour of the circuit described above, we are again solving for four coupled ODE's: one for each channel and one for the membrane voltage V_m. However, to obtain the desired spiking behaviour as displayed in Figure 7, it is sufficient to only solve for g_{slw} and U_m and set $g_\pm = g_{\pm,\infty}$.

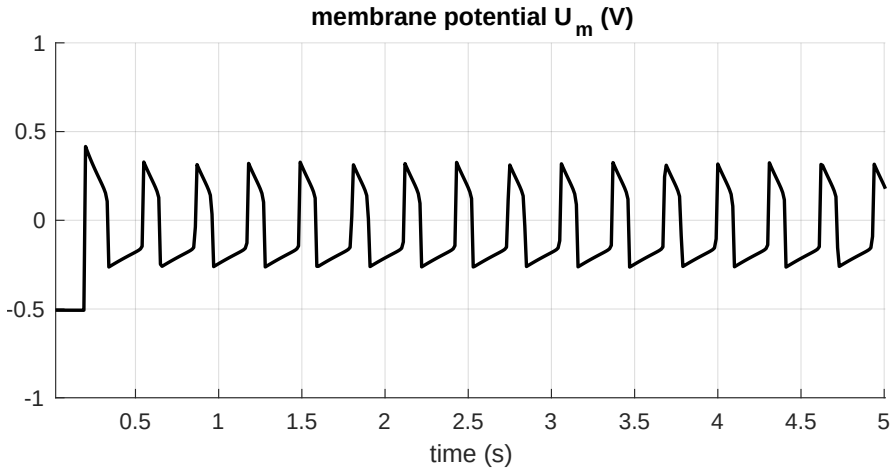

Figure 7: Spiking behaviour displayed by the iontronic Hodgkin-Huxkley-type circuit, analogous to spike trains of action potentials displayed by neurons. parameters?

It is insightful to make a phase-portait of this system when the spiking occurs. As we can now treat this circuit as a two dimensional dynamical system, this is neatly displayed in the $g_{slw} - U_m$-graph of Figure 8. It now becomes clear that the periodic limit cycle that is the periodic spike comes from the correct intersection of two nullclines given by

$$(\frac{\mathrm{d}g(t)}{\mathrm{d}t}, \frac{\mathrm{d}U_m(t)}{\mathrm{d}t}) = 0, \tag{5.2}$$

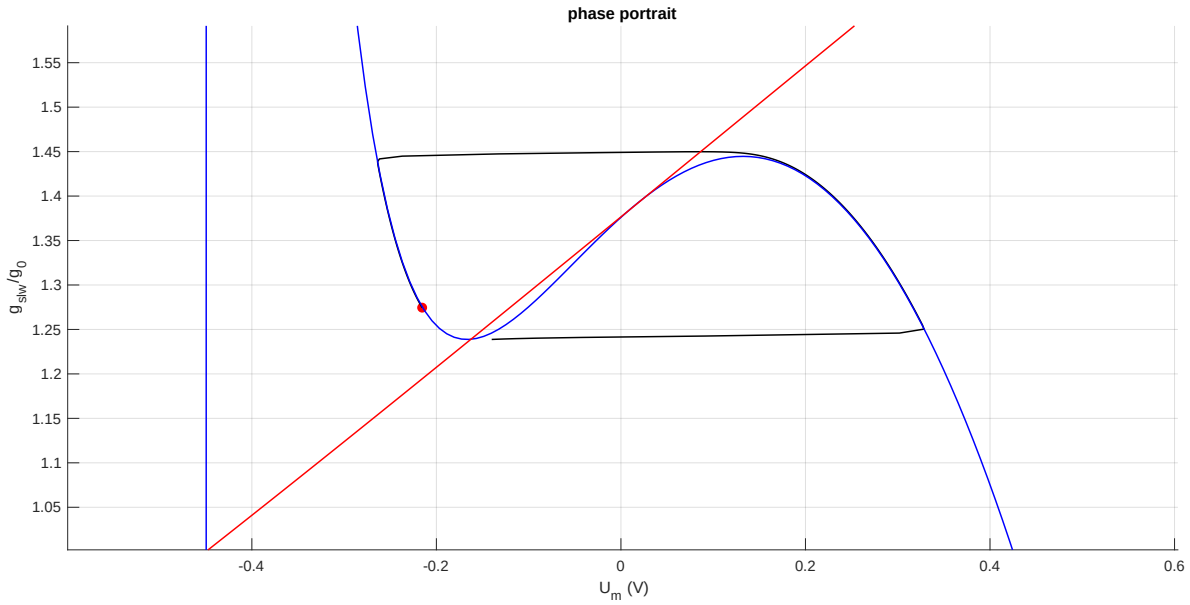

Figure 8: The phase portrait of a two-dimensional iontronic Hodgkin-Huxley type circuit displaying a typical periodic orbit. The periodic orbit occurs when the two nullclines intersect each other between the two extrema of the U_m-nullcline.

The individual nullclines are drawn in the phase-portrait. It is immediately clear that the periodic orbit lies on two-shoulders of the U_m-nullcline (blue), with a rapid transition between them. This only occurs when the g-nullcline (red) intersects it between its two extrema. Thereby, any change in parameter that makes the intersection fall in or outside this regime can be described as a Hopf bifurcation, with the creation of a limit cycle. The limit-cycle in the g-U plane represents our spike. By adding more dimensions to this system, for example by adding another channel with an even longer timescale, it is possible to create potentially more complex dynamical behaviour than simple tonic spiking, but that is outside the scope of this thesis. We will now go on to look at different ways to use conical microchannels to mimic some of the brain's other fundamental features.

6 Synapse Models

One way to model a synapse is to create a physical device that replicates the behavior of a synapse. This can involve building a device that has the same physical structure as the synapse, with channels and receptors for ions and neurotransmitters, or a simpler device that captures some of the electrochemical properties of natural synapses. The latter will be the focus of this section.

One of the key features of synapses is their *plasticity*, which is the ability of the synapse to change its strength in response to earlier activity. *Strength* typically refers to how likely and by how much a presynaptic spike will cause a postsynaptic spike, as a postsynaptic neuron often needs some minimum level of external forcing from its numerous connections to cross the spiking threshold. This associativity between neurons is widely believed to be central to memory and learning, although a detailed description of neural encoding is still missing [31] (for a longer discussion, see Section 3). Hence it is desirable, when creating synapse models, to incorporate such features, especially when it comes to making neuromorphic hardware, that has a similar distributed information storage approach as the brain[32]. For example, the model should be able to increase or decrease the strength of the synapse depending on the activity of the presynaptic and postsynaptic neurons. By incorporating these rules into the design of the model, we can create a device that replicates aspects of the behavior of the synapse.

Understanding synaptic plasticity can be useful when building neural networks, as it can provide insight into how networks of neurons can learn and adapt to new situations. By incorporating rules that govern synaptic plasticity into the design of a neural network, we can create networks that are more flexible and adaptable, and that can learn from experience more effectively, without the use of extensive and expensive global supervision. This can be especially useful for building neural networks that are used for tasks that require a lot of flexibility while operating on real time.

Memristors have been used to represent some parameters or information in neuromorphic computing. However, our type of memristor differs from the ones commonly used: it is volatile. This means, that after driving the system in a certain way, the signal is quickly erased as the device returns to the same equilibrium state as before the driving occurred. In this paragraph, we will explore a potential way to make the response of the conical microchannels to stimulation less volatile. Specifically, we a new semi-independent way to tune them on a time-scale much longer than the diffusive timescale, which is the timescale at which ion accumulation occurs and recedes (see Section 4). For this, we will use surface chemistry, which turns out to be a very fruitful feature to add to ionic memristors, opening up a pathway to many new neuromorphic functions.

To start with, we will use some adsorptive reaction

$$S + A^- \rightleftarrows SA^-, \tag{6.1}$$

where negative ions A^- adsorb and desorb on and from a neutral surface groups S on the channel wall of the microchannel. This equilibrium reaction can be described as a Langmuir process

$$\partial_t \sigma = k_F(\Gamma - \sigma) - k_B\sigma \tag{6.2}$$

with a total forward rate of $k_F = k_{adsorb}\rho_A(R)$ and a backward rate of $k_B = k_{desorb}$. We must include the concentration $\rho_A(R)$ specifically at the channel wall where the reactions occur, as this might be significantly different from bulk concentrations due to electrostatic interactions. Here, we take the ~~amount~~ of charged surface groups to be σ and the total amount of surface groups Γ. See Figure 9 for an illustration of this device. Without any external forcing, this reaction will equilibrate ($\partial_t\sigma = 0$) to

number

per unit area

why k_+ introduced, k_A and k_B are "physical" parameters?

$$\sigma_{eq} = \frac{\Gamma}{1 + \frac{k_B}{k_F}} \tag{6.3}$$

Note that we express σ and Γ in units of inverse surface area, such that the true surface charge is $e\sigma$ (with unit em^{-2}). Furthermore, k_F and k_B have units s^{-1}. In practice, it is not always known what the absolute values of these constants are for a certain adsorption reaction, as often only their relative rate k_B/k_F is known by measuring σ_{eq}. Throughout the rest of the project, we freely pick the relative rate such that the equilibrium surface potential is between 50 and 100 mV and the absolute rates to be significantly longer than the diffusive rate τ^{-1}.

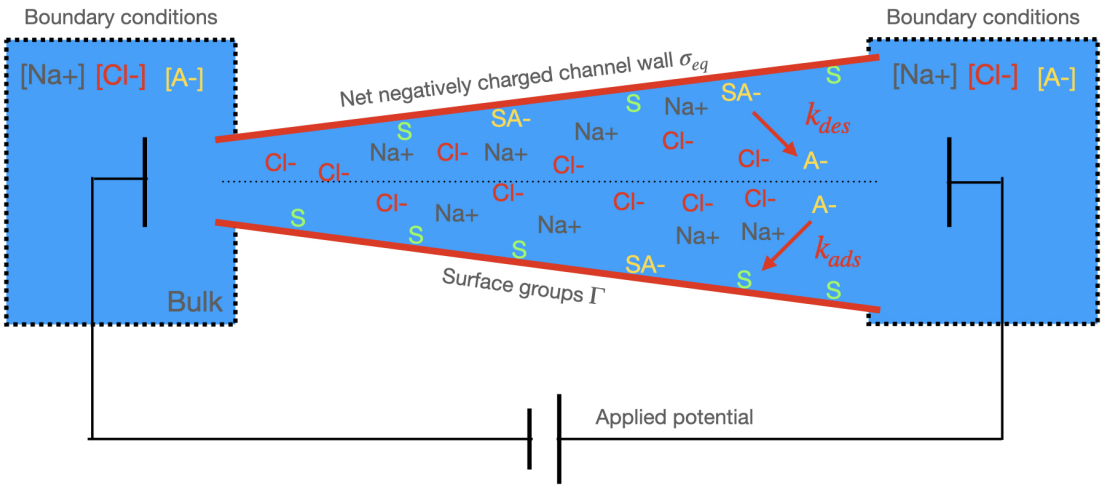

Figure 9: A schematic representation of the simulated conical microchannel with an active adsorption process at the channel wall. The reaction follows Langmuir kinetics.

When a microchannel in equilibrium is subsequently forced by an external applied electric potential, the concentration of reactive anions at the channel wall will start to vary, due to the same diffusive-electric effect that gives rise to the hysteresis loop described in section 4. However, this change in concentrations will then lead to a new equilibrium surface charge σ^*_{eq}, to which the system will develop. If this effect is large enough and the channel radii are small enough compared to the Debye length for the conductance of the electric double layers to be non-negligible compared the total conductance, we have obtained a new way to tune the conductance of the pore. This tuning can occur on a separate timescale, as will be displayed next.

6.1 A demonstration

The mechanism described in the previous section will be demonstrated here for a conical channel with a length of $L = 1\mu m$, a base radius $R_b = 120mm$ and tip radius $R_t = 30mm$ (for the full parameter set, see Appendix I). This value of $\frac{R_b}{R_t}$ is close to the optimal value for salt accumulation [29]. Inside the channel, we put a 1:1:1 electrolyte with a monovalent positive and negative conductive ion as well as a monovalent negative reactive ion. Far from the channel, we impose the concentrations to be equal to the bulk concentrations $\rho_{+,b} = 1mM$, $\rho_{-,b} = 0.98mM$ and the reactive anionion ρ_A, b at $0.02mM$, where these values are chosen to maintain global charge neutrality in the bulk of the fluid.

Upon stimulation with a pulse of $-1.2V$ (a negative value means the base is negatively charged with respect to the tip), the concentration profiles of all ions inside the cone will start to change. As a result, the concentration of reactive ions at the channel wall change, which in turn drives a change in the surface charge. An illustration of this charging process is shown in Figure 10 which show some snapshots of the charging process and illustrates how the surface charge profile follows after the concentration profile. In Figure 11, the voltage dependence of this phenomenon is displayed through the steady-state surface charge profile at different applied potentials. As we see, the surface charge is tuneable through the value of the applied potential.

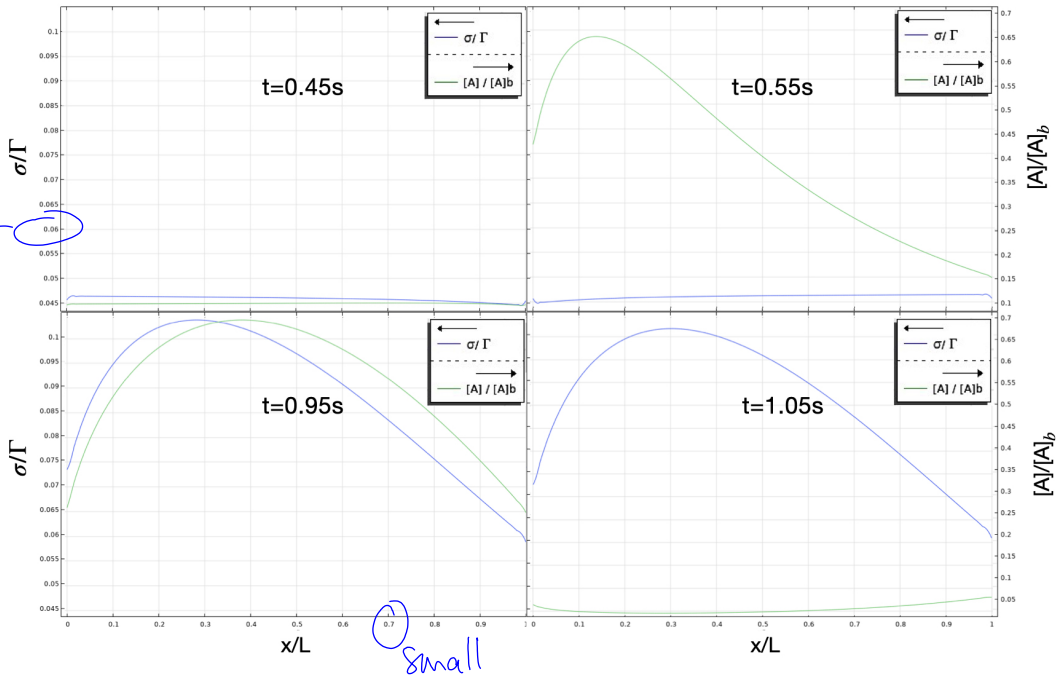

Figure 10: The response of the concentration profiles (tip to base) of the reactive ions and the surface charge to a voltage pulse of -1.2V between 500ms and 1000ms. Standard parameter set as stated in Appendix I.

As has been derived by Boon et al. (2022), the rates at which this charging and subsequent discharging occurs when the reactive ions and the charge surface repel each other are non-trivial and asymmetric. Using their results, inserting the Boltzmann distribution and assuming non-overlapping electric double layers, we obtain a prediction for the discharging rate written in terms of $s = \frac{\bar{\sigma}}{\bar{\sigma}_{eq}}$:

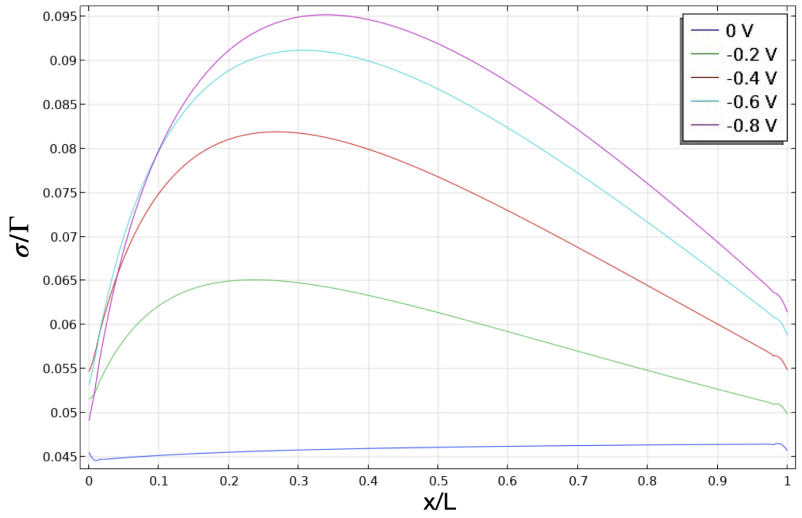

Figure 11: The equilibrium surface charge profile on the channel wall (base to tip) as a result of an external applied potential, expressed in terms of the total fraction of charged surface groups.

$$\begin{aligned}\partial_t s &= \rho_A(R) k_A\left(s^{-1} - s^{-2}\right) + k_B\left(s - s^{-2}\right) \\ &= \bar{\rho}_A \exp\left(\frac{e\Delta V_s}{k_b T}\right) k_A\left(s^{-1} - s^{-2}\right) + k_B\left(s - s^{-2}\right). \end{aligned} \tag{6.4}$$

This is in accordance with the findings of our finite-element simulations, shown in Figure 12a. In this figure, we use a Forward Euler time-stepping method initialised at t=1.0s to solve equation 6.4, and compare it to FE results. In the 12b, the effect on the conductance is shown as well, which follows a similar pattern but also shows the direct effect of ion accumulation on the conductance (blue). In order for the surface charge increase (green) to change the total conductance significantly, the channel radii need to be of the same order of magnitude as the Debye length, such that the conductance of the electric double layer significantly contributes to the total conductance. Note that in these figures, we simulate small measure pulses of -10mV to extract the conductivity from the FE simulations.

Already, we see that the retention time of the surface-charge increase is much higher than that of the ion accumulation (Figure 12b), as the effect of the ion accumulation decays at the diffusive timescale τ_D at the end of the voltage pulse. Interestingly, the discharging rate is also lower than the charging rate, as the effect persists much longer than the time needed for the charge to build up (500ms). This relatively long discharging time follows from the fact that during the pulse, the concentration of reactive ions is much higher relative to after the pulse, leading to a faster reaction rate. It is also aided by the slow discharging rate intrinsic to an adsorption reaction of a charged ion to a charged wall with the same sign[29]. Note that this is a somewhat counter-intuitive symmetry breaking of an otherwise symmetrical equilibrium reaction, and that the charging dynamics of a reaction like Equation 6.1 deserve a study of its own, which we will not do here. In the next section, we will explore methods to get a more extreme asymmetry between charging and discharging, by using substitution reactions and ions with a higher valency.

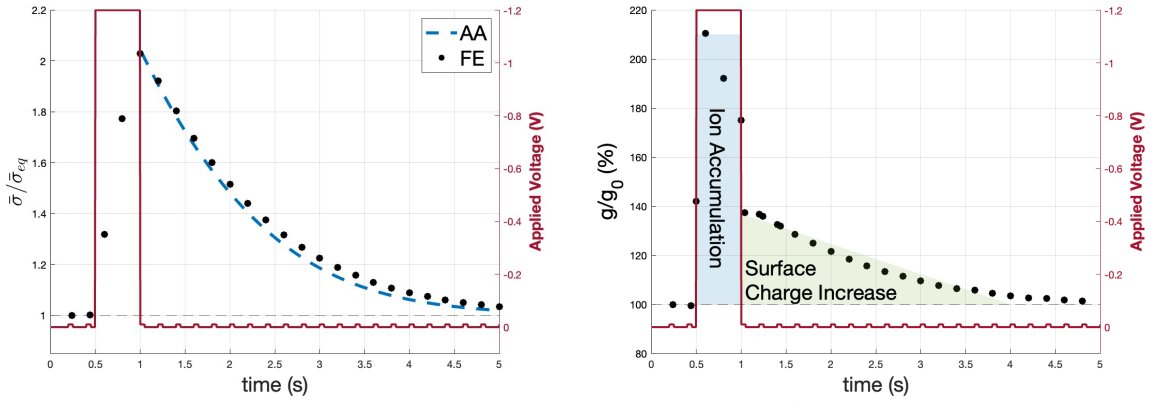

(a) (b)

how defined? stab-average? area-average?

Figure 12: The response of the average surface charge (a) and conductance (b) of a conical microchannel (L = 1μm, Rb = 120nm, Rt=30nm) with an adsorption reaction at the channel wall to a 500ms voltage pulse. The adsorptive ion has the same charge as the channel wall. The effect of the increased surface charge on the conductance decays much slower than the effect of the ion accumulation.

6.2 Substitution Reactions

Substitution reactions of the type

$$SB + A^{Z_A} \rightleftarrows SA^{Z_A - Z_B} + B^{Z_B} \tag{6.5}$$

, where Z_i represents the valency of ion i, can result in a much more non-linear charging dynamics due to the fact that both the forward and the backward reaction depend on the availability of an ion which is now attracted or repelled from the surface [29]. This is represented by the presence of a ρ_i term in both the forward and the backward rate of the Langmuir-type equation describing the kinetics at a point at the channel wall:

$$\begin{aligned} \sigma_t &= k_F(\Gamma - \sigma) - k_B\sigma; \\ k_F &= k_f \rho_A(R); \\ k_B &= k_b \rho_B(R). \end{aligned} \tag{6.6}$$

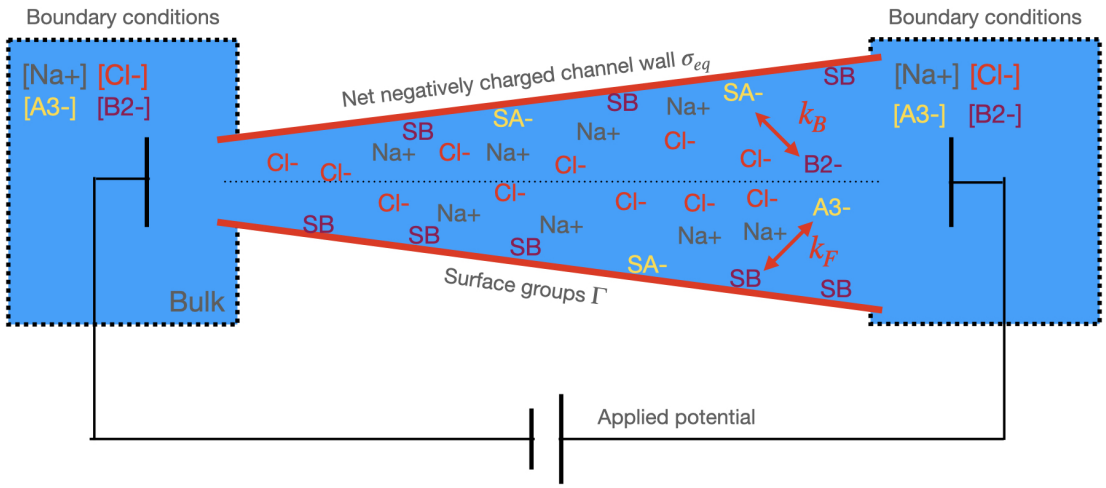

Figure 13: A schematic representation of a conical microchannel with an active subsitution reaction at the channel wall, following langmuir kinetics. The ionic species present in the channel are Na^+, Cl^-, B^{2-} and A^{3-}.

This creates the potential to strongly increase the retention time of the conductance change of a microchannel following electric stimulation. In this section, we will model a cone with such a substitution reaction, where both ρ_A and ρ_B at the reservoir boundaries are taken to be $0.02mM$, much smaller than the concentration of screening ions ρ_{Na} and ρ_{Cl} (1.0 mM $\pm\rho_{A/B}Z_{A/B}$, see Appendix I). A schematic representation of this system is given in Figure 13. The Figures 14 and 15 show the change in conductance following electric stimulation of two cones identical to the previous section, but with a substitution reaction on the channel wall.

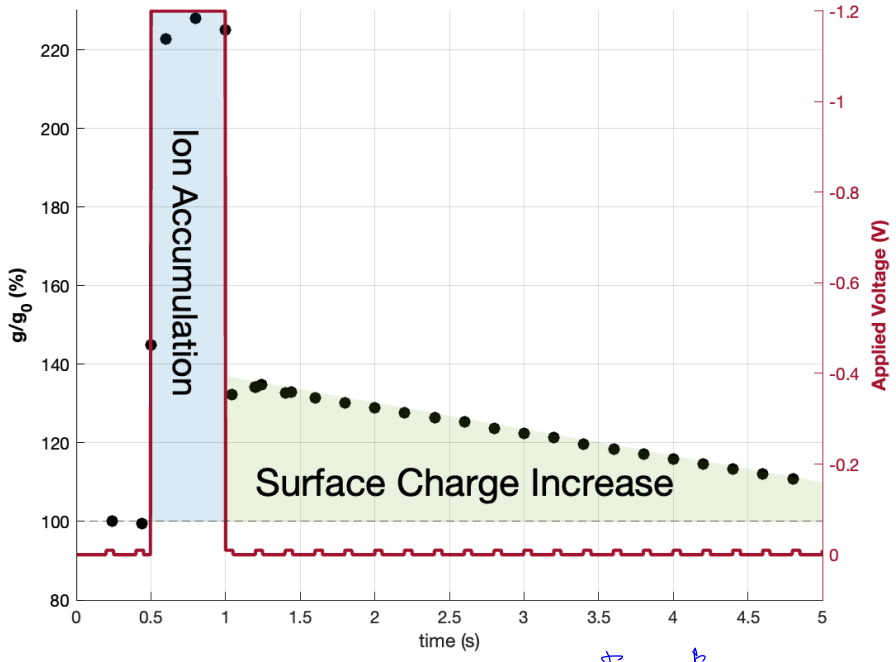

Figure 14: The conductance-response of a conical microchannel (L = 10μm, Rb = 120nm, Rt=30nm, see Appendix I) with a 2:1 substitution reaction at the channel wall to a 500ms voltage pulse. Both reactive ions have the same charge as the wall. The effect of the increased surface charge on the conductance (green) decays much slower than the effect of the ion accumulation (blue).

As can be seen in these figures, the retention time of this process is very large, and the cones in fact discharge much slower than they charged up. Notably, the diffusive time-scale of this system is still $\tau_D \approx 10ms$ (see insert of Figure 15). Since this is the typical time in which the effects of ion accumulation on the conductance will appear and decay. However, the timescale of the decay of the surface charge in the 3:2 surface reaction is approximately $\tau_S = 50s$, significantly longer than the pulse duration.

A comparison between the two figures also shows that the reaction with a trivalent and a divalent ion has a much longer retention time compared to the divalent and monovalent reaction. This is to be expected, as the supercharged surface strongly repels these divalent and trivalent ions, making it difficult to discharge when the electric pulse and ion accumulation have receded.

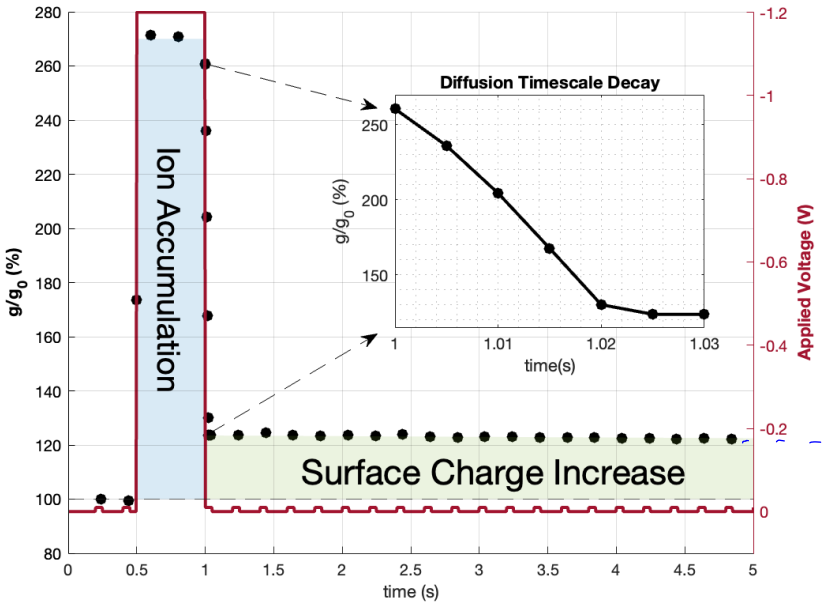

Figure 15: The conductance-response of a conical microchannel (L = 10μm, Rb = 120nm, Rt=30nm, see Appendix I) with a 3:2 substitution reaction at the channel wall to a 500ms voltage pulse. Both reactive ions have the same charge as the wall. The effect of the increased surface charge on the conductance (green) has an extremely long retention time compared to the diffusive timescale (blue) at which the ion accumulation recedes, as displayed in the insert.

Although the asymmetry between the charging and discharging rate can be intuitively understood using our knowledge of salt accumulation and nonlinear dynamics, the fact that the equilibrium surface charge changes at all during electric stimulation actually depends on a further fact. Both reactive ions will increase in total average concentration ($\langle \bar{\rho}_i \rangle$) by approximately the same amount, which would leave the equilibrium surface charge largely unchanged. However, as salt concentrations increase, there are more ions available to screen the surface charge in an electric double layer. The Boltzmann distribution $\rho_{A/B}(r)$ depends on the *surface potential*, and not the *surface charge*. The surface potential for a 1:1 electrolyte is given by the Gouy Chapman theory and can be derived as

$$\Delta U_s(x) = \frac{-2k_bT}{e} \sinh^{-1}(2\pi\sigma(x)\lambda_d(x)\lambda_b), \tag{6.7}$$

where we take into account that all these value depend on the distance along the cone, as a consequence of inhomogeneous concentration profiles. Since our Na^+ and Cl^- do the majority of the screening, and the reactive ions are only available in lower concentrations, we expect this relation to still hold for our system. As salt concentrations increase, the Debye length

$$\lambda_d(x) = \sqrt{\frac{\epsilon k_b T}{2e^2 \sum(\rho_i(x) Z_i^2)}}$$

will decrease. From the Boltzmann distributions of A and B, assuming identical concentration at $r = 0$, we can derive that

$$\frac{\rho_A(R)}{\rho_B(R)} = \exp\left\{\frac{(Z_B - Z_A)e\Delta U_s}{k_bT}\right\} = \exp\left\{\frac{e\Delta U_s}{k_bT}\right\}. \tag{6.8}$$

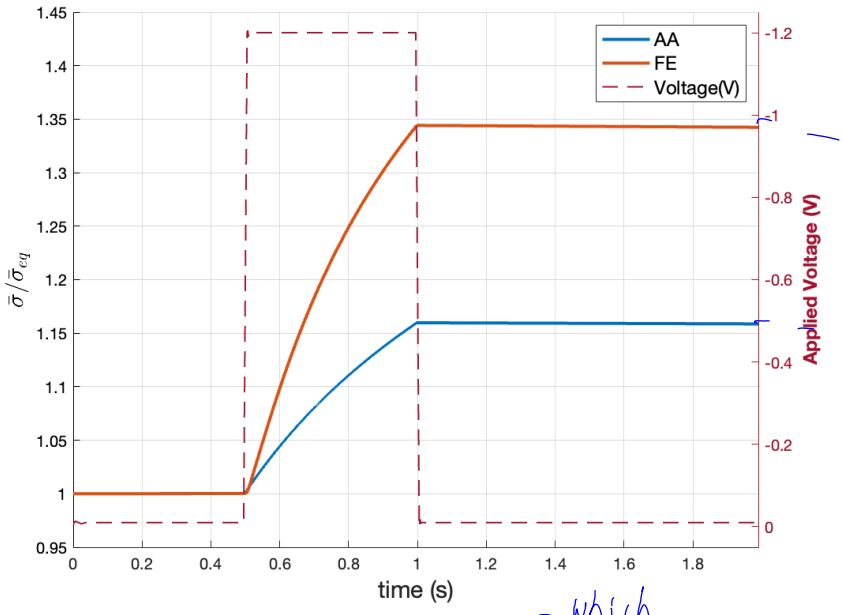

Figure 16: A comparison of an analytical approximation (AA) and a finite element (FE) simulation of the response of a conical microchannel (L = 1μm, Rb = 120nm, Rt=30nm) with a 3:2 repulsive substitution reaction to a 500ms voltage pulse.

Since in our case, the surface potential is negative, a depolarization (decrease in its absolute value) will lead to a relative increase in A^{3-} compared to B^{2-}, which is the reason for the change in equilibrium surface charge. To test this explanation, we model the FE simulation by numerically solving $\rho_i(x, V)$ (given in section 4) and $\sigma(t)$ (B.2), taking into account the spatially dependent screening. The results can be seen in Figure 16. The FE and the analytical approximation are in good agreement, although the analytic model underestimates the charging rate. This is not surprising, as the equations for the concentration profiles $\rho_i(x, V)$ do not describe out-of-equilibrium systems and assume homogeneous surface charge, as well as the lubrication limit of thin double layers. The sign and order of magnitude, as well as the fast charging and slow discharging are captured well, strengthening our hypothesis about the working of this system. For a more elaborate discussion of the analytical approximation, see Appendix II.

6.3 Chemically induced long term depression and Hebbian Learning

As described in Section 3, both signalling and plasticity in the chemical synapse are influenced by the presence of ions such as Na^+, K^+, Cl^- and Ca^{2+} as well as neurotransmitters. Thus far, we have only looked at ion concentrations as playing a passive role in the changes in conductance of our conical channel, following the actively controlled electric potential. However, an advantage of fully ionic devices compared to fully electronic ones, is that there is a much larger bandwidth of possible signals travelling through our microchannels. As we have multiple independent ionic species in our channel, we can change not only electric potentials driving an electric current, but also chemical ones driving an independent flux of chemical species.

There can be strong gradients in the concentrations of ions across neuronal membranes. For example, at rest, the concentration of potassium ions is roughly 30 times larger inside than outside of the cell [33]. The influx of positive ions along their concentration gradient is the main driver behind the generation of the action potential and, in the case of Ca^{2+}, the release of neurotransmitters by the presynaptic neuron. In the postsynaptic neuron, an influx of calcium ions is widely believed to play a decisive role in triggering LTP and LTD, with moderate increases leading to LTD and strong prolonged increases leading to LTP [26].

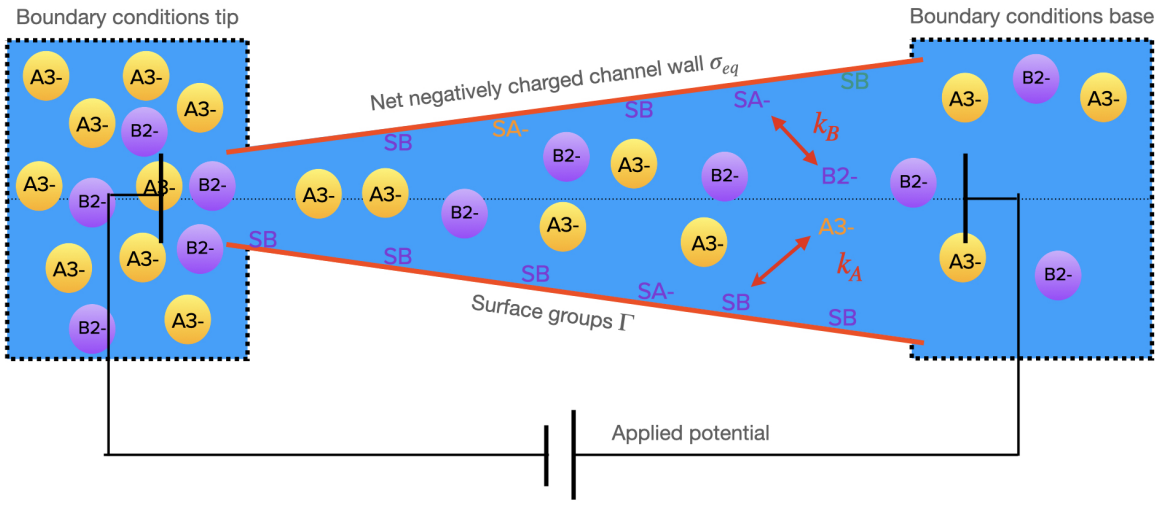

Figure 17: A schematic representation of a cone with a substitution reaction on the channel wall. Here, we apply not only an electric potential gradient, but also a concentration gradient, with the concentrations of our reactive ions much larger in the reservoir on the tip side compared to the reservoir on the base side. Screening ions (which are much more abundant than the reactive ions) are left out for clarity.

Interestingly, conical microchannels can mimic such effects. By applying concentration gradients between the tip and the base of the cone (Figure 17), we can strengthen, weaken and even reverse the effects of an electric pulse on the surface charge. In figure 19, we show an example of the reversed effect, a *Long Term Depression*. This channel is almost identical to the one displaying *Long Term Potentiation* in Figure 15, but has an applied concentration gradient. In this case, the boundary

condition concentration at the base-side $\rho_{A,b}$ is $4 \cdot 10^{-4} mM$ compared to $\rho_{A,t} = 2 \cdot 10^{-2} mM$ at the tip side. Applying this concentration gradient affects the ion accumulation during the electrical pulse such, that the equilibrium surface charge decreases instead of increases (Figure 18). This, in turn, decreases the conductance of the channel by up to 30% with a relatively long retention time. This mimics how different calcium concentrations across the postsynaptic membrane can influence the onset of LTP or LTD.

The effects of concentration gradients on the conductive properties and ionic fluxes in inhomogeneous microchannels deserves a study of its own and falls outside the scope of this thesis. For now, it is enough to note that concentration gradients have a large effect on the exact shape of our concentration polarization curves, which can in turn drive the surface charge profile.

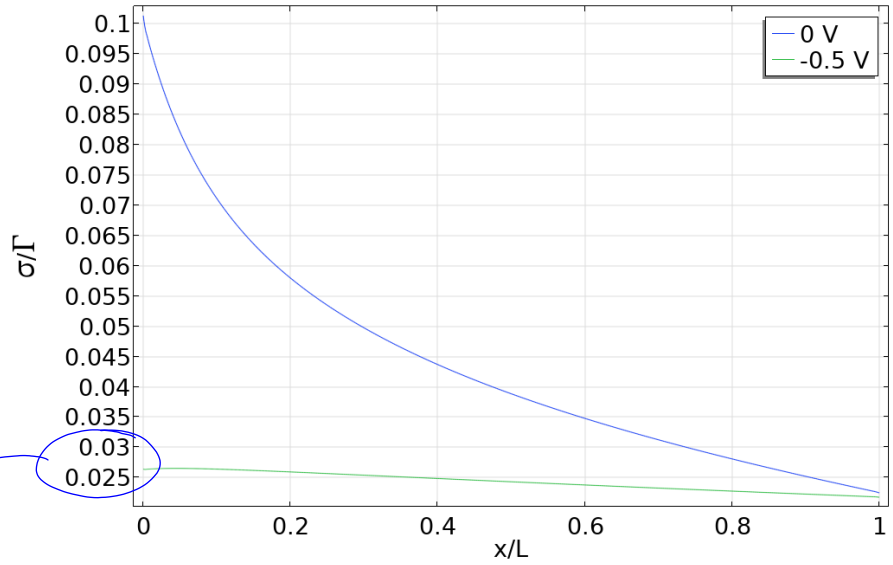

Figure 18: When applying a concentration gradient for the trivalent reactive ion, the response of the surface charge of a conical channel with a substitution reaction can change sign. Here, the cone has the standard parameter set as in Appendix I, but with a concentration $\rho_A = 4 \cdot 10^{-4}$ at the base reservoir.

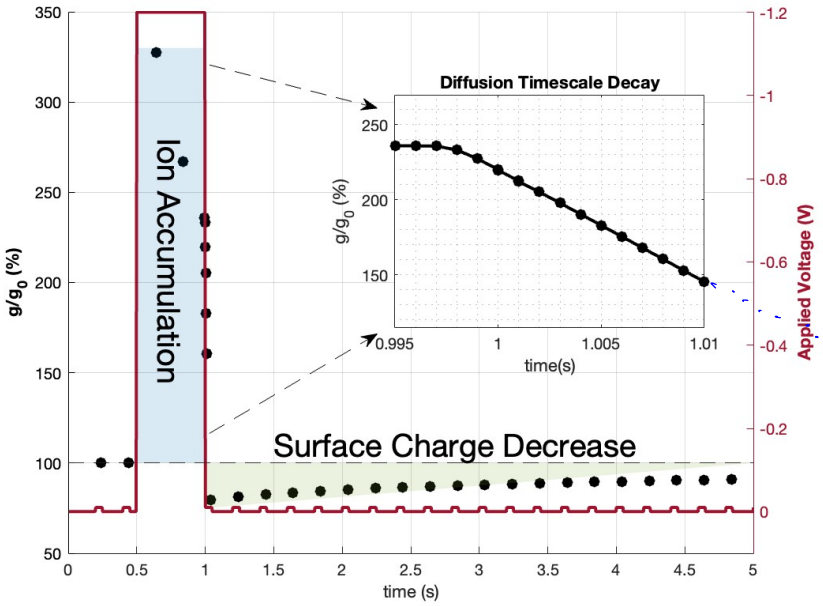

Figure 19: The conductance-response of a conical microchannel (L = 10μm, Rb = 120nm, Rt=30nm) with a 3:2 substitution reaction at the channel wall to a 500ms voltage pulse. Both reactive ions have the same charge as the wall. A steep gradient is applied to the trivalent ion, which has a concentration fifty times smaller at the channel tip compared to the base, while the divalent ion only has a twofold concentration decrease from base to tip reservoirs. There is a persistent drop in the conductance, with a decay rate much larger than the diffusive decay rate of the ion accumulation process.

Let us look at an interesting example of the effects of time-dependent changes in the concentration, as opposed to merely stationary gradients. We can mimic the electro-chemical processes that happen at the post-synaptic domain during pre- or post-synaptic activation. In the section on Synaptic Plasticity, we described the coincidence-detection mechanism of the NMDA receptor. This ion channel only opens when there is both a chemical signal, in the shape of an increase in available neurotransmitters, as well as a sufficiently strong depolarization of the postsynaptic neuron. The NMDA receptor, which is highly permeable to Ca^{2+}, is believed to play an important role for plasticity. We can mimic its functionality by constructing a conical channel that only increases in conductance when both electric and chemical activation occur at the same time. An demonstration of this is shown in Figure 20. Between 0.5 and 1.0s, either the voltage-, the concentration gradient or both are altered, and we can see that a strong change in conductance only occurs when both are present.

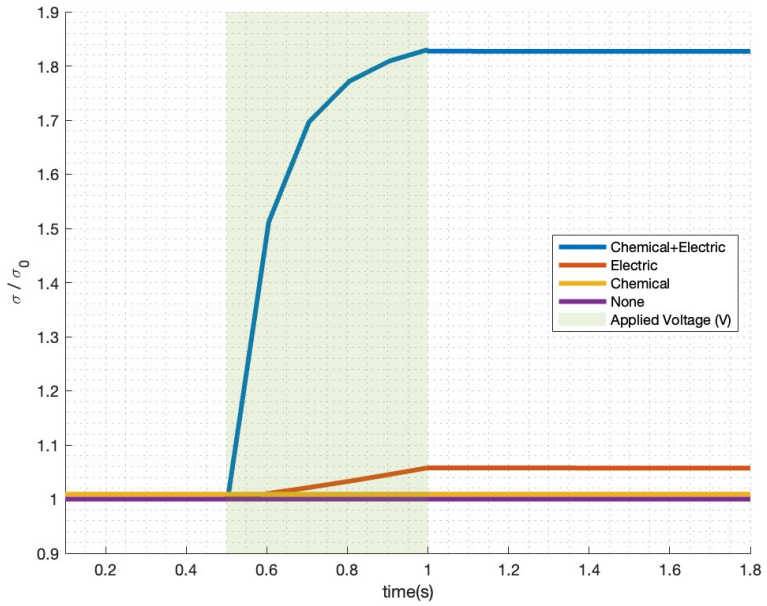

Figure 20: The response of the surface charge of a conical channel with a 3:2 substitution reaction to different types of stimulation. An electric pulse corresponds to a -1.0V electric potential gradient and a chemical pulse corresponds to a raising of the concentration of reactive ions at the base reservoir ($1e-3mM$ to $1e-2mM$). The pulses occur between 500ms and 1s (green).

During this simulation, the relative concentration ρ_A/ρ_B is kept constant, but both are elevated by a factor 10 at the base-end of the cone in the case of a chemical signal, from $4 \cdot 10^{-3} mM$ to the standard $2 \cdot 10{-}2 mM$. This increase in concentration leaves the equilibrium surface charge in-tact, but leads to an increase in effective reaction rate. To make the analogy with synaptic signalling explicit, a chemical signal (concentration increase) corresponds to presynaptic activity and a concurring release of neurotransmitters. An electrical signal corresponds to a depolarization of the postsynaptic neuron (an action potential). Both signals are assumed to occur simultaneously. In the study of Spike Time Dependent Plasticity (STDP), temporal differences between these signals would be of particular interest. In reality, the relative strengthening and weakening of the synaptic strength would depend on the exact timing of the neurotransmitter release and the speed at which neurotransmitters are taken up and removed from the synaptic cleft.

If we put the last two results together, we see that it is possible with a chemical pulse to temporarily change the response of the conical channel ~~to an electric pulse~~. For that, we perform the same FE simulation as in Figure 20, but now we change ρ_A/ρ_B during the pulse. We start with the standard parameter set, but with $\rho_A = 4 \cdot 10^{-4} M$ at the base reservoir. During the pulse, we only increase ρ_A at the base reservoir to $1 \cdot 10^{-2} M$. As we can see in Figure 21 we now have a device that lowers its surface charge (and conductance) upon electrical stimulation only, increases its surface charge upon chemical stimulation only, and strongly increases its surface charge upon coincident chemical and electric stimulation. Here we see a strong analogy with the NMDA coincidence detection mechanism, with LTD, 'facilitation' and LTP during post-, pre- and simultaneous synaptic activity respectively.

These results neatly demonstrate the potential for neuromorphic, synapse-like plasticity in conical microchannels with substitution reactions. As not only electric but also chemical potentials can influence the conductance state of this device, we have opened up the possibility for many types

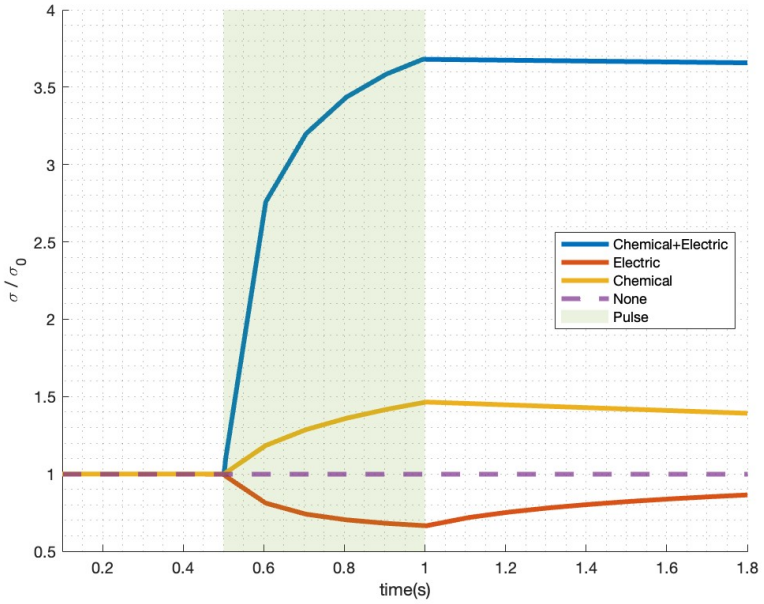

Figure 21: The response of the avarage surface charge of a cone with a 3:2 substitution reaction at the channel wall. Full parameter set given in Appendix I, with the following alteration: at rest, the concentration of the trivalent reactive ion is decreased fifty times at the base reservoir. During a chemical pulse, it is increased to only half the standard value ($1 \cdot 10^{-2} mM$. An electrical pulse corresponds to a -1.0 V electric potential.

of exploitation of non-linear transport phenomena.

In the previous parts of this section, we have described how to tune the conductance state of our conical microchannels with electric and chemical signals of different signs and magnitudes. We will now look at a different type of plasticity mentioned in Section 3: frequency dependent plasticity.

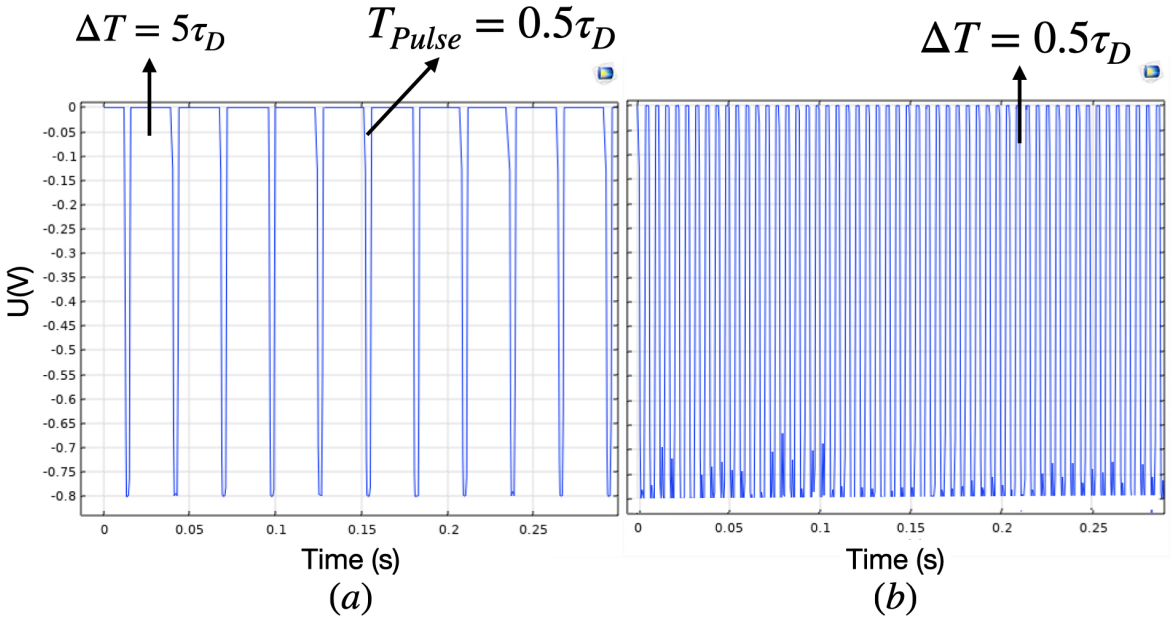

Figure 22: Pulse trains with different frequencies but similar pulse-widths and an amplitude of -0.8V. The studied regime ranges from $\Delta T < \tau_D$ to $\Delta T > \tau_D$, such that subsequent pulses build or do not build up their effects on the conical channels, respectively

6.4 Frequency dependent plasticity

In hippocampal and cortical neurons, different stimulation paradigms of a pre-synaptic neuron are known to lead to different relative amounts of LTP/LTD. That is, synapses respond differently to an incoming pulse train of 100Hz compared to an incoming pulse train of 5Hz, where the former is usually associated with strengthening (LTP) of the synapse, and the latter with weakening (LTD) [34].

Interestingly, the device described in the previous paragraphs, can display frequency-dependent plasticity of some kind too. As we have a process which is highly volatile (the accumulation of salt) and another coupled process which is much more stable (the change in surface charge), we can find long-term effects of differences in frequency. The basic mechanism is as follows: If voltage spikes follow each other closely, their effect on the salt concentrations will add up, whereas if there is a lot of time between voltage spikes, the increase in salt concentration following one pulse will have been erased before the next one arrives. Since different salt concentrations can lead to different equilibrium surface charges, we expect a cone stimulated with a fast frequency to charge to a higher σ_{eq} than a cone stimulated with a lower frequency.

To demonstrate this mechanism, let us simulate the experiment described above. We define the duration of a voltage pulse as τ_p and the time in between pulses as ΔT such that the frequency is $f = 1/(\tau_p + \Delta T)$. We'll then only vary ΔT to simulate a synapse being activated by pulse trains with different rates, with the time between pulses ranging from $\Delta T < \tau_D$ to $\Delta T > \tau_D$. The cones will be similar to those described in the previous section, with a 1:1:3:2 electrolyte, and the latter two being reactive ions present at low concentrations. See Appendix I for the full parameter set. The charging rates are also increased to reduce the simulation time needed for the surface charge to reach an equilibrium, with $k_f = 200 s^{-1} m M^{-1}$ and $k_b = 300 s^{-1} m M^{-1}$.

As we can see in Figure 23, different frequency pulse trains lead to different asymptotic surface

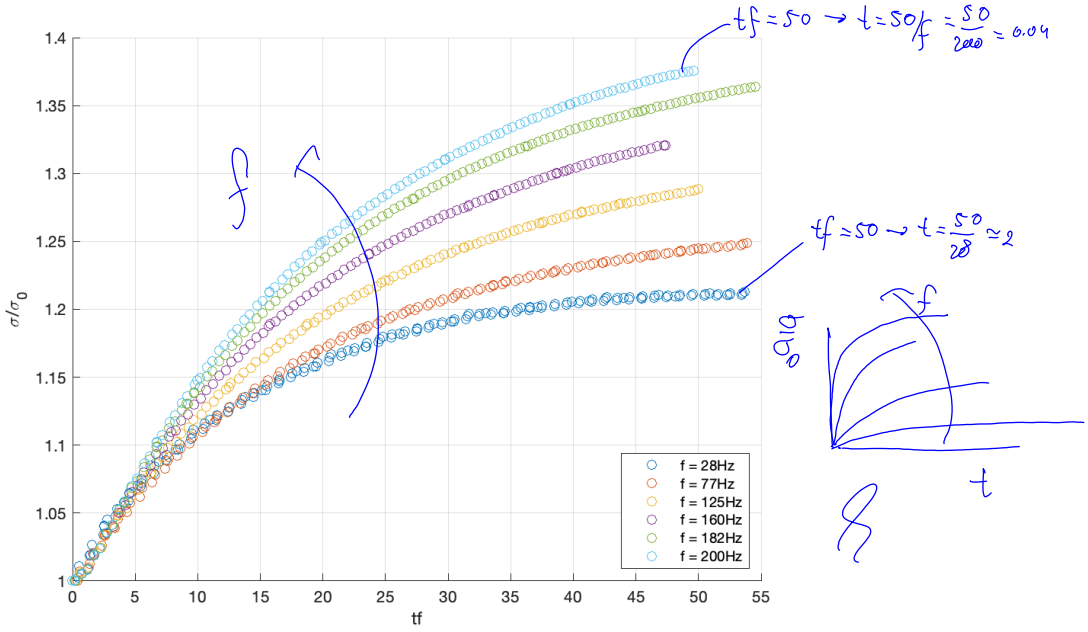

Figure 23: The response of a conical channel with active surface chemistry in response to pulse trains with varying frequencies. The time axis is scaled by the frequency of the different pulse trains in Hz, such that every point on a vertical line has had an equal number of pulses. Dimensions are similar to the Standard Parameter Set, but with $k_f = 200s^{-1}mM^{-1}$ and $k_b = 300s^{-1}mM^{-1}$.

charges, emulating one of the synaptic plasticity rule. Figure 24 shows the corresponding response of the conductance of the channel. We see that higher frequencies lead to higher asymptotic conductances. A further step would be to combine this with previous results, to try and construct a device that lowers its surface charge at low frequencies, and increases them at higher, but this is outside the scope of this thesis, as we just aim to demonstrate these fundamental features.

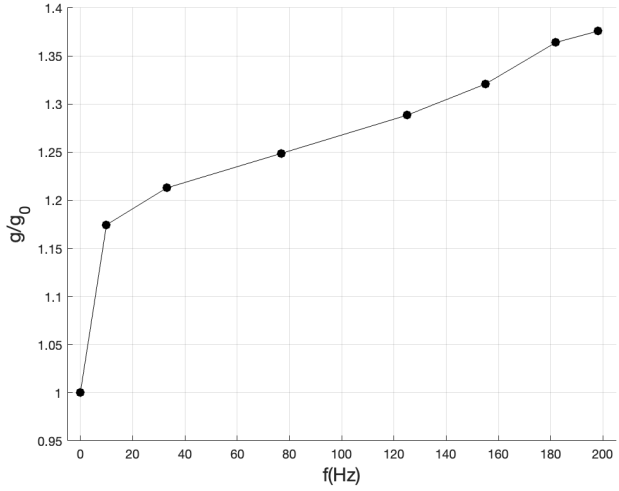

Figure 24: The conductance of a conical microchannel with active surface chemistry depends on the frequency of the spike train running through it.

7 Outlook, Conclusion and Discussion

summary?

7.1 Outlook: Temporal and Spatial Addition in Spiking Neural Networks

So far, we have investigated action potentials and plasticity. There are, however, other important fundamental characteristics of signal transmission and computation in the brain. In particular, it is important to study how neurons process the incoming signals. Our previous neuron model already showed an all-or-nothing spiking response, but the question of what the scalar input I represents, we have left untouched.

refer to section?

At the dendrite of a neuron, incoming action potentials and excitatory postsynaptic potentials (EPSPs) can be temporally and spatially added together to produce a composite signal. Action potentials are rapid, all-or-nothing electrical signals that are generated by neurons and propagate along their axons. EPSPs, on the other hand, are slower, graded potentials that are generated by the flow of ions across the cell membrane at the synapse [17].

these are "loose" statements, perhaps more suitable for introduction

Temporal summation refers to the process by which action potentials and EPSPs that arrive at the dendrite closely in time are summed together, resulting in a stronger composite signal. Spatial summation, on the other hand, refers to the process by which action potentials and EPSPs that arrive at different locations on the dendrite are summed together, again resulting in a stronger composite signal.

Artificial neural networks (ANNs) are computing systems that are inspired by the structure and function of the brain. In ANNs, the process of temporal and spatial summation is typically simulated using mathematical equations that describe the flow of signals between the neurons. While these equations can be effective for modeling certain aspects of the behavior of neurons, they do not always accurately reflect the complex, nonlinear behavior of real neurons [35].

Spiking neural networks (SNNs) are a type of neural network that are designed to more closely mimic the behavior of real neurons. In SNNs, each neuron is modeled as a dynamical system that can exhibit complex, nonlinear behavior [36]. This behavior is influenced by factors such as the flow of ions across the cell membrane, the release of neurotransmitters, and the activity of other neurons that the cell is connected to. By using this more biologically realistic model of the neuron, SNNs can better capture the process of temporal and spatial summation at the dendrite of a real neuron. This can be useful for tasks such as pattern recognition or decision making, where the ability to accurately model the behavior of neurons is important.

how, why? reference?

A promising application for the results shown in this thesis would be to construct networks that combine the spiking and plasticity behaviour in a network architecture that can perform unsupervised learning tasks. In the study of SNNs dynamical systems that are supposed to mimic synapses are normally made out of solid state devices [37], but the devices presented here would be a good candidate for the construction of iontronic spiking neural networks.

7.2 Conclusion and Discussion

The use of microfluidics in conical microchannels is promising for the construction of novel neuromorphic devices. In the previous sections, we have seen how the processes of salt accumulation and depletion, together with Langmuir-Kinetics-driven reactive surfaces, can lead to neuromorphic behaviour such as long-term memory, spiking and plasticity under the right experimental paradigms. Many of the effects reported here are novel and still speculative. Numerical finite-element and analytical modelling lends itself well for the discovery of interesting physical mechanisms and optimal parameter sets. However, experimental verification is required to see if these mechanisms can actually be meaningfully exploited to the extent suggested here.

The types of surface chemistry present in our modelled conical microchannels are theoretical: we freely chose our reaction rates and ion valencies to demonstrate the desired effect as clearly as possible. A specific surface reaction with relevant forward and backward rates will need to be found in the literature of surface chemistry. One such example is the calcium charging of silica groups ($SiOH + Ca^{2+} \rightleftarrows SiOCa^{+} + H^{+}$). However, the literature of surface chemistry is somewhat obscure, and lists of all known surface reactions with their respective absolute forward and backward rates do not exist. Luckily, there is a lot of room for exploring interesting parameter spaces by easily varying the amount of surface groups as well as the absolute and relative concentrations of all ions.

It is important to note that some of the systems described above involve divalent and trivalent ions, for which mean field theories generally break down. These systems fall in the regime of *Strong Coupling Theory*, with a coupling parameter significantly larger than one [38]. In this case, particle-particle interactions become so strong, that mean field theories such as Poisson Boltzmann theory break down [38] as strong correlations between the positions of the charged particles appear. It is not yet clear if the results are therefore significantly skewed, as our trivalent and divalent ions are co-ions to the surface and they occur in small concentrations compared to the conductive ions, not raising the ionic strength $I = \frac{1}{2}\sum_i \rho_i Z_i^2$ by more than 10%. Experimentally, it is possible to further experiment with different ion radii and ion concentrations to find which regimes show interesting behaviour similar to the effects displayed here.

As our double layers are mainly made up of our screening ions, the specific concentration profiles of our reactive ions are not important for the conductance of our devices. For the charging kinetics to be modelled accurately, we only need accurate values of the concentrations at the channel wall. All in all, we expect most of the predicted absolute values for charging strength and speed to be significantly different in real life, but we also expect the effects to be relatively robust. Experimental validation is needed to see if these results qualitatively hold up in real-life settings.

This investigation of reactive surfaces in conical microchannels for computing or sensing purposes probably only comprises a small part of what is possible to do with these devices. The possibility to signal with electric, chemical and pressure signals through fluidic microchannels lends itself to many more experimental set-ups. In this thesis, we have only looked at constant and alternating electrical signals, with or without chemical signals. The interplay with pressure, which is know to influence the flow and current rectification of these channels, has not been explored yet.

Further work could focus on exploring different plasiticity and learning rules. There are a large amount of such rules known in biological and computational neuroscientific literature, however, the methods to model or replicate them artificically are still being developed [39]. Further refining the analogy between spike-time-dependent plasticity and the behaviour of the chemically active conical microchannels is one potential avenue. Different types of 3-factor learning rules could also be explored. The focus on STDP and FDP in this report was chosen purely for demonstration.

Additionally, further investigations into useful networks and other architectures that could be made with these microchannels are warranted. This is largely unattainable through Finite Element methods such as COMSOL, and would require good analytical approximations, which is why we have tried to construct those in section 6. One goal could be to build networks that display a type of associative memory, resembling a Hopfield Network or a spiking neural network, as described in the previous paragraph. Since the microchannels can change their conductance states purely based on previous inputs and respond non-trivially to different electrochemical signals, these microchannels are highly suitable for such approaches.

define, ref?

References

- inconsistent : title slanted, journal name straight & vv

1. Luka, G. *et al.* Microfluidics integrated biosensors: A leading technology towards lab-on-a-chip and sensing applications. *Sensors* **15,** 30011–30031 (2015).
2. Dittrich, P. S. & Manz, A. Lab-on-a-chip: microfluidics in drug discovery. *Nature reviews Drug discovery* **5,** 210–218 (2006).
3. Pol, R., Céspedes, F., Gabriel, D. & Baeza, M. Microfluidic lab-on-a-chip platforms for environmental monitoring. *TrAC Trends in Analytical Chemistry* **95,** 62–68 (2017).
4. Stone, H. A. & Kim, S. Microfluidics: basic issues, applications, and challenges. *American Institute of Chemical Engineers. AIChE Journal* **47,** 1250 (2001).
5. Merlet, C. *et al.* The electric double layer has a life of its own. *The Journal of Physical Chemistry C* **118,** 18291–18298 (2014).
6. Nie, B., Li, R., Brandt, J. D. & Pan, T. Iontronic microdroplet array for flexible ultrasensitive tactile sensing. *Lab on a Chip* **14,** 1107–1116 (2014).
7. Hou, Y. & Hou, X. Bioinspired nanofluidic iontronics. *Science* **373,** 628–629 (2021).
8. Yu, L. *et al.* Bioinspired Nanofluidic Iontronics for Brain-like Computing. *Nano Research* (2023).
9. Ciresan, D. C., Meier, U., Masci, J., Gambardella, L. M. & Schmidhuber, J. *Flexible, high performance convolutional neural networks for image classification* in *Twenty-second international joint conference on artificial intelligence* (2011).
10. Nassif, A. B., Shahin, I., Attili, I., Azzeh, M. & Shaalan, K. Speech recognition using deep neural networks: A systematic review. *IEEE access* **7,** 19143–19165 (2019).
11. Katz, D. M., Bommarito, M. J., Gao, S. & Arredondo, P. Gpt-4 passes the bar exam. *Available at SSRN 4389233* (2023).
12. Bojarski, M. *et al.* End to end learning for self-driving cars. *arXiv preprint arXiv:1604.07316* (2016).
13. Mittal, S. & Vaishay, S. A survey of techniques for optimizing deep learning on GPUs. *Journal of Systems Architecture* **99,** 101635 (2019).
14. Chua, L. Memristor-the missing circuit element. *IEEE Transactions on circuit theory* **18,** 507–519 (1971).
15. Hecht-Nielsen, R. *Theory of the backpropagation neural network* in *Neural networks for perception* 65–93 (Elsevier, 1992).
16. Qiao, N. *et al.* A reconfigurable on-line learning spiking neuromorphic processor comprising 256 neurons and 128K synapses. *Frontiers in neuroscience* **9,** 141 (2015).
17. Kandel, E. R. *et al. Principles of neural science* (McGraw-hill New York, 2000).
18. Emes, R. D. & Grant, S. G. Evolution of synapse complexity and diversity. *Annual review of neuroscience* **35,** 111–131 (2012).
19. Ho, V. M., Lee, J.-A. & Martin, K. C. The cell biology of synaptic plasticity. *Science* **334,** 623–628 (2011).
20. Cragg, B. G. The density of synapses and neurons in normal, mentally defective ageing human brains. *Brain: a journal of neurology* **98,** 81–90 (1975).
21. Markram, H., Gerstner, W. & Sjöström, P. J. Spike-timing-dependent plasticity: a comprehensive overview. *Frontiers in synaptic neuroscience* **4,** 2 (2012).
22. Karmarkar, U. R. & Buonomano, D. V. A model of spike-timing dependent plasticity: one or two coincidence detectors? *Journal of neurophysiology* **88,** 507–513 (2002).

23. Timmermans, W, Xiong, H, Hoogenraad, C. & Krugers, H. Stress and excitatory synapses: from health to disease. *Neuroscience* **248,** 626–636 (2013).
24. Köhr, G. NMDA receptor function: subunit composition versus spatial distribution. *Cell and tissue research* **326,** 439–446 (2006).
25. Lüscher, C. & Malenka, R. C. NMDA receptor-dependent long-term potentiation and long-term depression (LTP/LTD). *Cold Spring Harbor perspectives in biology* **4,** a005710 (2012).
26. Xia, Z. & Storm, D. R. The role of calmodulin as a signal integrator for synaptic plasticity. *Nature Reviews Neuroscience* **6,** 267–276 (2005).
27. Boon, W. Q., Veenstra, T. E., Dijkstra, M. & van Roij, R. Pressure-sensitive ion conduction in a conical channel: Optimal pressure and geometry. *Physics of Fluids* **34** (2022).
28. Aarts, M. *et al.* Ion Current Rectification and Long-Range Interference in Conical Silicon Micropores. arXiv:2206.14594 [cond-mat, physics:physics]. `http://arxiv.org/abs/2206.14594` (2022) (Oct. 2022).
29. Boon, W., Dijkstra, M. & van Roij, R. Coulombic surface-ion interactions induce non-linear and chemistry-specific charging kinetics. arXiv:2210.15426 [cond-mat, physics:physics]. `http://arxiv.org/abs/2210.15426` (2022) (Oct. 2022).
30. Izhikevich, E. M. *Dynamical systems in neuroscience* (MIT press, 2007).
31. Martin, S. J., Grimwood, P. D. & Morris, R. G. Synaptic plasticity and memory: an evaluation of the hypothesis. *Annual review of neuroscience* **23,** 649–711 (2000).
32. Schuman, C. D. *et al.* Opportunities for neuromorphic computing algorithms and applications. *Nature Computational Science* **2,** 10–19 (2022).
33. Rienecker, K. D., Poston, R. G. & Saha, R. N. Merits and limitations of studying neuronal depolarization-dependent processes using elevated external potassium. *ASN neuro* **12,** 1759091420974807 (2020).
34. Mayford, M., Wang, J., Kandel, E. R. & O'Dell, T. J. CaMKII regulates the frequency-response function of hippocampal synapses for the production of both LTD and LTP. *Cell* **81,** 891–904 (1995).
35. Buonomano, D. V. Decoding temporal information: a model based on short-term synaptic plasticity. *Journal of Neuroscience* **20,** 1129–1141 (2000).
36. Ghosh-Dastidar, S. & Adeli, H. Spiking neural networks. *International journal of neural systems* **19,** 295–308 (2009).
37. Boyn, S. *et al.* Learning through ferroelectric domain dynamics in solid-state synapses. *Nature communications* **8,** 14736 (2017).
38. Netz, R. R. Electrostatistics of counter-ions at and between planar charged walls: From Poisson-Boltzmann to the strong-coupling theory. *The European Physical Journal E* **5,** 557–574 (2001).
39. Khacef, L. *et al.* Spike-based local synaptic plasticity: A survey of computational models and neuromorphic circuits. *arXiv preprint arXiv:2209.15536* (2022).
40. Ali, M., Mafe, S., Ramirez, P., Neumann, R. & Ensinger, W. Logic Gates Using Nanofluidic Diodes Based on Conical Nanopores Functionalized with Polyprotic Acid Chains. *Langmuir* **25.** Publisher: American Chemical Society, 11993–11997. ISSN: 0743-7463. `https://doi.org/10.1021/la902792f` (2022) (Oct. 2009).
41. Bouvier, M. *et al.* Spiking Neural Networks Hardware Implementations and Challenges: a Survey. *ACM Journal on Emerging Technologies in Computing Systems* **15.** arXiv:2005.01467 [cs], 1–35. ISSN: 1550-4832, 1550-4840. `http://arxiv.org/abs/2005.01467` (2022) (June 2019).

42. *Artificial Neural Networks and Machine Learning – ICANN 2021: 30th International Conference on Artificial Neural Networks, Bratislava, Slovakia, September 14–17, 2021, Proceedings, Part V* en (eds Farkaš, I., Masulli, P., Otte, S. & Wermter, S.) ISBN: 978-3-030-86382-1 978-3-030-86383-8. https://link.springer.com/10.1007/978-3-030-86383-8 (2022) (Springer International Publishing, Cham, 2021).

43. Janson, P., Gabrielsson, E. O., Lee, K. J., Berggren, M. & Simon, D. T. An Ionic Capacitor for Integrated Iontronic Circuits. en. *Advanced Materials Technologies* **4,** 1800494. ISSN: 2365-709X. (2022) (2019).

44. Li, J., Dong, Z., Luo, L., Duan, S. & Wang, L. A novel versatile window function for memristor model with application in spiking neural network. en. *Neurocomputing* **405,** 239–246. ISSN: 0925-2312. https://www.sciencedirect.com/science/article/pii/S0925231220307542 (2022) (Sept. 2020).

45. Lucas, R. A., Lin, C.-Y., Baker, L. A. & Siwy, Z. S. Ionic amplifying circuits inspired by electronics and biology. en. *Nature Communications* **11.** Number: 1 Publisher: Nature Publishing Group, 1568. ISSN: 2041-1723. http://www.nature.com/articles/s41467-020-15398-3 (2022) (Mar. 2020).

46. L. Werkhoven, B. & Roij, R. v. Coupled water, charge and salt transport in heterogeneous nano-fluidic systems. en. *Soft Matter* **16.** Publisher: Royal Society of Chemistry, 1527–1537. https://pubs.rsc.org/en/content/articlelanding/2020/sm/c9sm02144b (2022) (2020).

47. Mohamed, E., Josten, S. & Marlow, F. A purely ionic voltage effect soft triode. en. *Physical Chemistry Chemical Physics* **24,** 8311–8320. ISSN: 1463-9076, 1463-9084. http://xlink.rsc.org/?DOI=D1CP04581D (2022) (2022).

48. Sinha, A. *Evolving Nano-scale Associative Memories with Memristors* en. Tech. rep. (Jan. 2000). http://archives.pdx.edu/ds/psu/7371 (2022).

49. Wang, H., Li, C.-L., Banerjee, S. & He, S.-B. Novel memristor and memristor-based applications. en. *The European Physical Journal Special Topics,* epjs/s11734–022–00697–1. ISSN: 1951-6355, 1951-6401. https://link.springer.com/10.1140/epjs/s11734-022-00697-1 (2022) (Nov. 2022).

50. Yamazaki, K., Vo-Ho, V.-K., Bulsara, D. & Le, N. Spiking Neural Networks and Their Applications: A Review. en. *Brain Sciences* **12.** Number: 7 Publisher: Multidisciplinary Digital Publishing Institute, 863. ISSN: 2076-3425. https://www.mdpi.com/2076-3425/12/7/863 (2022) (July 2022).

51. Arbring Sjöström, T. *et al.* A decade of iontronic delivery devices. *Advanced Materials Technologies* **3,** 1700360 (2018).

52. Boybat, I. *et al.* Neuromorphic computing with multi-memristive synapses. *Nature communications* **9,** 1–12 (2018).

53. Fang, X., Duan, S. & Wang, L. Memristive FHN Spiking Neuron Model and Brain-Inspired Threshold Logic Computing. *Neurocomputing* (2022).

54. Izhikevich, E. M. Simple model of spiking neurons. *IEEE Transactions on neural networks* **14,** 1569–1572 (2003).

55. Robin, P., Kavokine, N. & Bocquet, L. Principles of Hodgkin-Huxley iontronics with two-dimensional nanofluidic memristors. *arXiv e-prints,* arXiv–2105 (2021).

56. Robin, P *et al.* Long-term memory and synapse-like dynamics of ionic carriers in two-dimensional nanofluidic channels. *arXiv preprint arXiv:2205.07653* (2022).

57. Xu, W., Wang, J. & Yan, X. Advances in memristor-based neural networks. *Frontiers in Nanotechnology* **3,** 645995 (2021).

58. Kamsma, T., Boon, W., Spitoni, C & van Roij, R. Unveiling the capabilities of bipolar conical channels in neuromorphic iontronics. *Faraday Discussions* (2023).

A Parameter Sets

Table 1 presents the standard parameter set used for Figures 3-5.

Parameter	Value	Unit
Length	10	μm
R_b	200	nm
R_t	50	nm
$\rho_{\pm}$	0.5	mM
σ	-1e17	e/m^2
D	1.5e-9	m$^2/s$
T	293	K

Table 1: Figure 3-5

Table 2 presents the parameter set used in the Hudgking Huxley-type circuit corresponding to and used to generate Figures 5-7.

Parameter	Value	Unit
L$_{\pm}$	2.5	μm
L$_{slw}$	10	μm
R_b	200	nm
R_t	50	nm
$\rho_{\pm}$	0.5	mM
σ	-1e17	e/m^2
D	1.5e-9	m$^2/s$
C$_m$	1e-15	F
I$_{app}$	1.3e-13	A
E$_{slw}$	-0.45	V
E$_{\pm}$	0.75	V
T	293	K

Table 2: Figure 5-7

Table 3 shows presents the parameter set used for the simulation of conical channels with an adsorption reaction on their channel wall. Cone dimensions are reduced to increase effects of double layer on channel conductance.

Parameter	Value	Unit
L	1	μm
R_b	120	nm
R_t	30	nm
ρ_+	1.0	mM
ρ_-	0.98	mM
ρ_A	0.02	mM
Z_A	-1	1
Γ	1e18	$1/\mathrm{m}^2$
D	1.5e-9	m^2/s
k_{adsorb}	10	$\mathrm{mM}^{-1}\mathrm{s}^{-1}$
k_{desorb}	0.4	s^{-1}
T	293	K

Table 3: Figures 10-12

Table 4 shows the standard parameter set used for the simulation of conical channels with a substitution reaction on their channel wall with either a combination of di- and monovalent reactive ions or tri- and divalent reactive ions in Figures 15-23.

Parameter	Value	Unit
L	1	μm
R_b	120	nm
R_t	30	nm
ρ_+	1.0 + $Z_A\rho_A$	mM
ρ_-	1.0 - $Z_B\rho_B$	mM
$\rho_{A/B}$	0.02	mM
Z_A	-1/-2	1
Z_B	-2/-3	1
Γ	1e18	$1/\mathrm{m}^2$
D	1.5e-9	m^2/s
k_f	200	$\mathrm{mM}^{-1}\mathrm{s}^{-1}$
k_b	250	$\mathrm{mM}^{-1}\mathrm{s}^{-1}$
T	293	K

Table 4: Figures 15-23 (deviations described in specific captions)

B Notes on analytical approximation of conical microchannels with surface Langmuir Kinetics

Figure 16 features a comparison of the results from Finite Element methods and analytical approximation with time-stepping methods that make use of expressions derived for the physics of charged conical microchannels and Langmuir kinetics.

To get a better understanding of what physics is behind the strongly non-linear charging and discharging dynamics observed in the finite element methods and to test the hypothesis that this is largely driven by screening effects, we see how close our analytical approximation comes to the results from Finite Element analysis, and investigate where the errors could lie. For reference, we give a more elaborate account of the modelling steps here.

We will use a modified version of Equation 4.6 to calculate the laterally averaged concentration profiles of our different ionic species along the cone:

$$\rho_s(x,V) - 2\rho_b = \frac{\Delta\rho^*}{\mathrm{Pe}}\left[\frac{x}{L}\frac{R_\mathrm{t}}{R(x)} - \frac{e^{\mathrm{Pe(V)}\frac{x}{L}\frac{R_\mathrm{t}^2}{R_\mathrm{b}R(x)}} - 1}{e^{\mathrm{Pe(V)}\frac{R_\mathrm{t}}{R_\mathrm{b}}} - 1}\right]\mathrm{d}x/L, \tag{B.1}$$

Where we use a modified $\Delta\rho^* \equiv 2(\Delta R\sigma_0 + R_b\Delta\sigma)(e\Delta U_{s,tip}/k_bTR_t^2)$ with $\sigma_0 = \sigma(0)$ and $\Delta\sigma = \sigma(0.99L) - \sigma(0)$ to capture the effects of the inhomogeneous surface charge [58].

We assume all ions with different valencies to follow the same concentration polarisation, though FE simulations show up to 50% variation between concentrations of ions of different valencies at the center of the channel. Also, since we are interested in changes to the surface charge occurring on the order of hundreds of milliseconds or more, we assume the salt concentrations to instantaneously change upon application of an electric potential instead of modelling the diffusion process as in Equation 4.8.

As described in Section 6, we calculate not only spatially dependent transversely averaged concentrations, but also the spatially dependent Debye length λ_D and surface potential ΔU_s. We then assume a Boltzmann distribution for each ions transversal concentration profile, such that the value of the concentrations at the channel wall are $\rho_i(x) = \bar{\rho}_i(x)\exp\left\{\frac{-Z_ie\Delta U_s(x)}{k_bT}\right\}$. Note that this assumes thin double layers, which is not a good approximation at the tip of our cone, where $R_b \approx 5\lambda_D$.

Using timestepping, we then forward the following differential equation:

$$\begin{aligned}\sigma_t &= k_F(\Gamma - \sigma) - k_B\sigma; \\ k_F &= k_f\rho_A(R); \\ k_B &= k_b\rho_B(R).\end{aligned} \tag{B.2}$$

This gives us the results shown in Figure 16. The conclusion is that changes in surface potential through screening effects indeed largely explain the characteristic charging behaviour of this device. Multiple approximations were used that are not fully warranted, such as valency-independent concentration polarisation, linear surface charge profiles, stationary-state concentration profiles and the lubrication limit of thin electric double layers. More detailed and complicated models could better capture the magnitude of the surface charge change.